Contrib Mineral Petrol (2015) 170:20
DOI 10.1007/s00410-015-1171-2

ORIGINAL PAPER

An Early Cretaceous garnet pressure–temperature path recording synconvergent burial and exhumation from the hinterland of the Sevier orogenic belt, Albion Mountains, Idaho

Eric D. Kelly[1] · Thomas D. Hoisch[2] · Michael L. Wells[3] · Jeffrey D. Vervoort[4] · Mengesha A. Beyene[5]

Received: 12 January 2015 / Accepted: 10 July 2015

Abstract Rocks may undergo complex pressure–temperature (*P–T*) histories during orogenesis in response to alternating episodes of synconvergent burial and exhumation. In this study, chemical zoning in garnets combined with textural and chemical evidence from the schist of Willow Creek in the Albion Mountains of south-central Idaho (USA), reveals a complex *P–T* path during the early stages of Sevier orogenesis. The distribution of quartz inclusions combined with internal resorption features establishes a hiatus in garnet growth. Chemical zoning was simulated using a *G*-minimization approach to yield a *P–T* path consisting of three distinct pressure changes during increasing temperature, defining an "N" shape. Lu–Hf isochron ages from multiple garnet fractions and whole-rock analyses in two samples are 132.1 ± 2.4 and 138.7 ± 3.5 Ma. The samples were collected from the hanging wall of the Basin-Elba thrust fault and yielded results similar to those previously obtained from the footwall. This leads to several conclusions: (1) Both the hanging wall and footwall experienced the same metamorphic event, (2) the paths document a previously unrecognized crustal thickening and synorogenic extension cycle that fills an important time gap in the shortening history of the Sevier retroarc, suggesting progressive eastward growth of the orogen rather than a two-stage history, and (3) episodes of extensional exhumation during protracted convergent orogenesis are increasingly well recognized and highlight the dynamic behavior of orogenic belts.

Keywords Pressure–temperature path · Lu–Hf garnet geochronology · Sevier orogeny · Albion Mountains · Basin-Elba fault · Trace-element zoning

Introduction

Isochemical phase diagrams ("pseudosections") have been used in many studies to construct *P–T* paths by considering the inferred sequence of mineral assemblages and their *P–T* fields; a limitation of this approach is that it commonly requires an assumption that the remaining unknown portion of the path, for which the sequence cannot be inferred, is linear or clockwise in shape (e.g., Tinkham and Ghent 2005; Cirrincione et al. 2008; Stowell et al. 2011; Cutts et al. 2014; Nabelek and Chen 2014). More sophisticated techniques, based on chemical zoning in garnet that developed during garnet growth, can be used to extract more detailed *P–T* paths (e.g., Spear et al. 1984; Gaidies et al. 2008a; Moynihan and Pattison 2013a; Vrijmoed and Hacker 2014). Equilibrium thermodynamics predicts that changes in garnet composition during growth occur as a

Communicated by Timothy L. Grove.

Electronic supplementary material The online version of this article (doi:10.1007/s00410-015-1171-2) contains supplementary material, which is available to authorized users.

✉ Eric D. Kelly
Eric.Kelly@utexas.edu

[1] Department of Geological Sciences, University of Texas, Austin, TX 78712, USA

[2] School of Earth Sciences and Environmental Sustainability, Northern Arizona University, Flagstaff, AZ 86011, USA

[3] Department of Geoscience, University of Nevada, Las Vegas, NV 89154, USA

[4] School of the Environment, Washington State University, Pullman, WA 99164, USA

[5] Turner Fairbank Highway Research Center, Federal Highway Administration, McLean, VA 22101, USA

Published online: 05 August 2015

result of changes in the *P–T* conditions (e.g., Spear 1995). However, there can be complicating factors, such as crystallization histories in which periods of growth are interrupted by periods of consumption, changes in mineral assemblages and reactions during growth, temperature-dependent changes in garnet chemistry from intracrystalline cation diffusion, and the degree to which chemical equilibrium was attained upon garnet nucleation. This study provides an example in which all of these factors are considered in order to arrive at a robust *P–T* path.

Many geodynamic models of orogenesis predict clockwise *P–T* paths in the shape of a simple loop resulting from thrust burial, radiogenic heating, and extensional exhumation (e.g., England and Thompson 1984; Jamieson and Beaumont 2011). However, some petrologic studies show that metamorphic rocks can follow more complex paths in *P–T* space (Spear et al. 1984; Selverstone and Spear 1985; Spear et al. 1990; Florence and Spear 1993; Lang 1996; Zeh and Millar 2001; Hoisch et al. 2002; Harris et al. 2007; Gaidies et al. 2008b; Vorhies and Ague 2011; Wells et al. 2012; Moynihan and Pattison 2013b; Dorfler et al. 2014). Such complexity may reveal important aspects of tectonic history and orogenesis. Alternations in contraction and extension, commonly referred to as tectonic mode switches (e.g., Lister et al. 2001), may be triggered by various factors resulting in changes in gravitational potential energy, horizontal compressive stress, or rock strength (Platt 1986; England and Houseman 1989; Willett 1992; Rey et al. 2001) and may provide a framework for interpreting more complex *P–T* paths such as the one reported here.

Previously reported *P–T* paths based on garnet zoning have revealed alternations in thrusting and exhumation during Sevier orogenesis, documenting complex departures from the simple model of a clockwise *P–T* path (Hoisch et al. 2002; Harris et al. 2007; Wells et al. 2012). In this study, we determine a *P–T* path from amphibolite-facies pelitic schist in the northern Albion Mountains, Idaho, in the hinterland of the Sevier orogenic belt. Samples for this study come from the hanging wall of a major thrust, the Basin-Elba fault. We also report two garnet Lu–Hf ages that date the path. From the footwall, previous work has reported both a *P–T* path and garnet Lu–Hf ages (Harris et al. 2007; Cruz-Uribe et al. 2015). The results of the present study allow for a comparison between the footwall and hanging-wall *P–T* histories and an evaluation of the implications for Sevier orogenesis.

Geologic setting

The Albion Mountains are part of the Raft River–Albion–Grouse Creek metamorphic core complex, one of many that occur along a north–south trend in the western USA in the hinterland of the Sevier orogen (Fig. 1) (Armstrong 1968a; DeCelles 2004). Samples were collected in the northern Albion Mountains of southern Idaho, in the hanging wall of a major thrust, the Basin-Elba fault (BEF). The hanging wall consists of overturned Neoproterozoic to Cambrian middle amphibolite-facies quartzite and pelitic schist of the Mount Harrison sequence, which represent the lower limb of a major fold nappe (Miller 1983). The footwall consists of Neoproterozoic to Ordovician lower amphibolite-facies metasedimentary rocks of the Raft River Mountain sequence (Miller 1980, 1983) that unconformably overlie the Archean Green Creek complex (Armstrong 1968b). The fault zone comprises a complexly folded and sheared mixture of metasedimentary rocks (pelitic schist, graphitic schist, quartzite, and metacarbonate lithologies), and lower-grade slivers of Mississippian rocks that have been interpreted as evidence of late extensional reactivation (Miller 1983; Hodges and Walker 1992).

Exhumation of the western part of the core complex is partly attributed to extension along the Middle Mountain shear zone (Saltzer and Hodges 1988). Two episodes of extension have been proposed based on a Middle to Late Eocene top-to-the-west-northwest shear fabric and a Late Oligocene–Middle Miocene top-to-the-west fabric in the Grouse Creek and Albion Mountains (Wells et al. 2004). The BEF represents the only fault with a clear older-over-younger thrust relationship still preserved through Mesozoic and Tertiary extension in the region, and juxtaposes more than 3.4 km of Neoproterozoic to early Cambrian metasedimentary rocks over Proterozoic to Ordovician metasedimentary rocks; the low-angle fault separating the little-studied Robinson Creek sequence above from the Mount Harrison sequence below may also be a preserved thrust (Fig. 2).

Sample descriptions

Mineralogy

This study focuses on garnet schist from the middle schist member of the schist of Willow Creek (Miller 1983) in the hanging wall of the BEF (Fig. 2), in the lower limb of a fold nappe. Samples in this study were collected within 2 km of each other in a single structural block, roughly 2–3 km west of the trace of the BEF, and thus, it can be assumed that all samples shared the same *P–T* history.

The four samples studied are metapelites from three outcrops and contain the mineral assemblage quartz + muscovite + biotite + garnet + plagioclase + ilmenite and minor or trace amounts of staurolite, apatite, zircon, monazite, and tourmaline (Fig. 3; Table 1). Garnet porphyroblasts are up to about 2 mm in diameter in three samples and up to

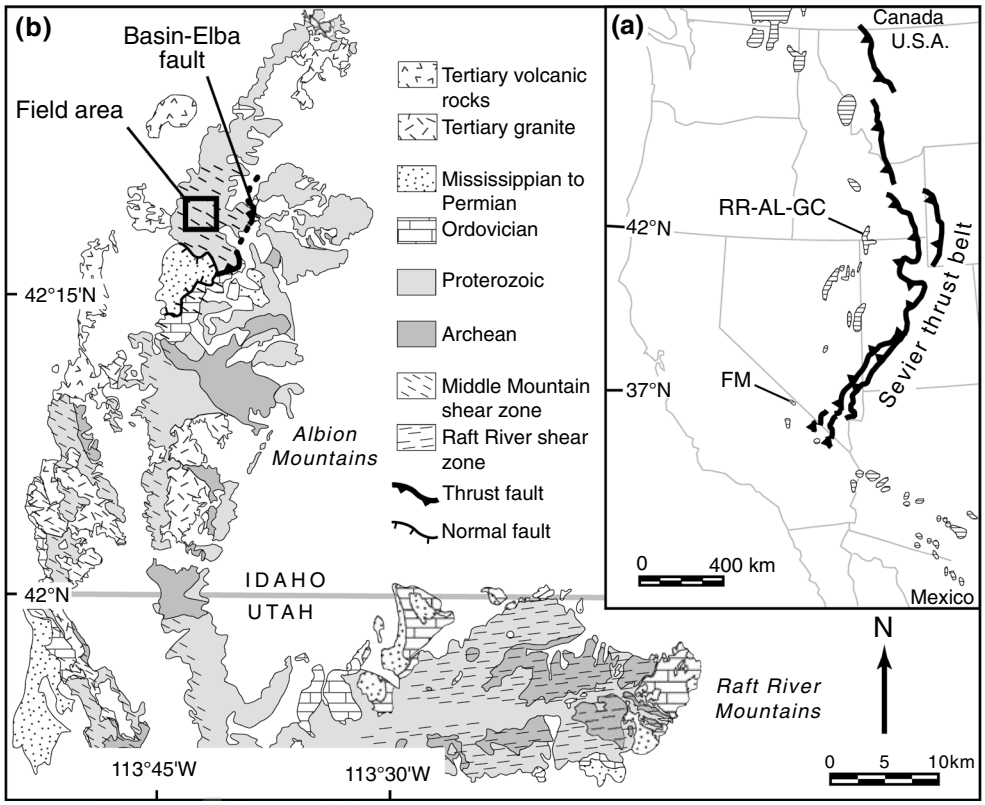

Fig. 1 Partial map of the Raft River–Albion–Grouse Creek (RR–AL–GC) metamorphic core complex. **a** The RR–AL–GC metamorphic core complex is part of a chain of Cordilleran metamorphic core complexes extending from Canada to Mexico (*horizontal line fill*) that lie west of the Sevier thrust belt (*black line with barbs*). *FM* Funeral Mountains. Core complexes modified from Armstrong (1982) and Camilleri and Chamberlain (1997). **b** Simplified geologic map of the Albion and Raft River Mountains showing the location of the field area in the hanging wall of the Basin-Elba fault. Modified from Hoisch et al. (2002)

about 4 mm in diameter in the fourth sample (EKAL29A). The garnets are subidioblastic to idioblastic, and most show inclusion-rich cores and inclusion-poor rims. Inclusions in garnet primarily consist of quartz and ilmenite with some apatite, zircon, monazite, and tourmaline grains.

One garnet crystal from each of the four samples was selected for analysis. In an effort to use crystal sections that capture the most complete history of chemical zoning from core to rim, the largest, most idioblastic grains were chosen from among 20–50 crystals per sample. Three of the chosen crystals exhibit evidence of near-central sectioning (high Y in center of crystal section), and the fourth shows evidence of sectioning farther from the core of the garnet (low Y in center of crystal section).

Element zoning in garnet crystals

Garnet line traverses, and spot analyses of muscovite, biotite, and plagioclase were generated using a Cameca MBX electron microprobe at Northern Arizona University. For all samples, the accelerating voltage was 15 kV. The beam current was 25 nA for garnet and 10 nA for all other minerals. The beam was focused for garnet (<1 μm) and defocused to 5 μm for all other minerals. Natural and synthetic standards were used for calibration. Garnets were traversed with a consistent point spacing of 20–40 μm. Poor garnet analyses were culled from the dataset and were attributable to cracks or overlaps with inclusions. The mineral analyses are given in Online Resources 1–4. Garnet major-element X-ray maps (Mg, Mn, Fe and Ca) were acquired using a JEOL JSM-6480LV scanning electron microscope with an Oxford EDS system at Northern Arizona University using an accelerating voltage of 20 kV and sample current of 50 nA. X-ray maps of Y were obtained using the electron microprobe (JEOL 8200 Superprobe) at The University of Texas at Austin. The accelerating voltage was 15 kV, the beam current was 1 μA, the dwell time was 200 ms, and the pixel size was 4–5 μm. The maps were enhanced by adjusting the brightness, contrast, and levels of the raw images using image processing software to emphasize the relatively high and low concentrations of each element.

All of the garnets display chemical zoning with decreasing mole fraction of spessartine (X_{sps}) from core to rim (Figs. 4, 5). Two of the garnets (ALMO13A and

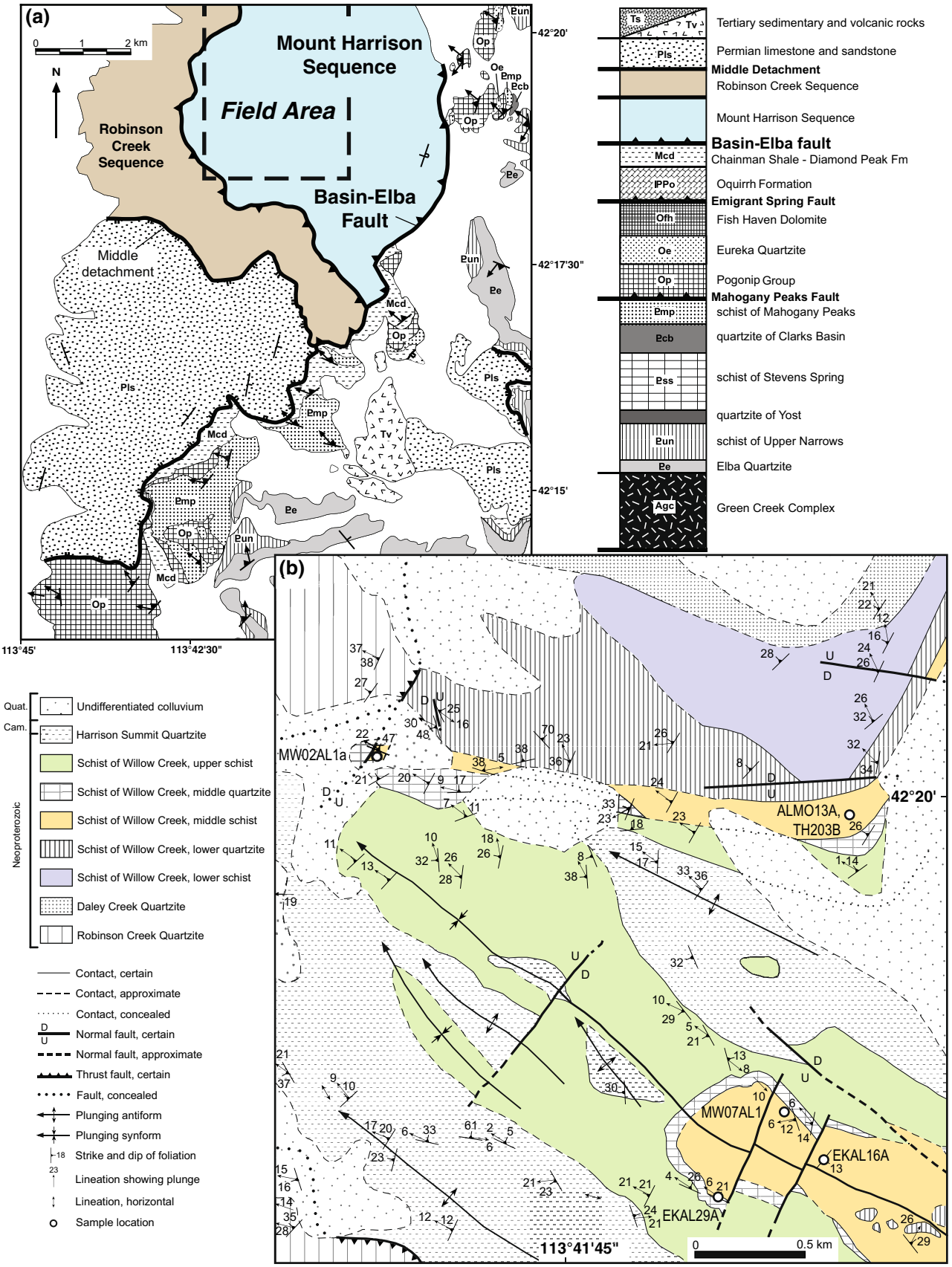
(a)
0 1 2 km
N
Mount Harrison Sequence
Field Area
Robinson Creek Sequence
Basin-Elba Fault
Middle detachment
42°20'
42°17'30"
42°15'
113°45'
113°42'30"
Ts
Tv
Tertiary sedimentary and volcanic rocks
Pls
Permian limestone and sandstone
Middle Detachment
Robinson Creek Sequence
Mount Harrison Sequence
Basin-Elba fault
Mcd
Chainman Shale - Diamond Peak Fm
IPPo
Oquirrh Formation
Emigrant Spring Fault
Ofh
Fish Haven Dolomite
Oe
Eureka Quartzite
Op
Pogonip Group
Mahogany Peaks Fault
Emp
schist of Mahogany Peaks
Ecb
quartzite of Clarks Basin
Ess
schist of Stevens Spring
quartzite of Yost
Eun
schist of Upper Narrows
Ee
Elba Quartzite
Agc
Green Creek Complex
(b)
MW02AL1a
ALMO13A,
TH203B
MW07AL1
EKAL16A
EKAL29A
42°20'
113°41'45"
0 0.5 km
Quat.
Cam.
Neoproterozoic
Undifferentiated colluvium
Harrison Summit Quartzite
Schist of Willow Creek, upper schist
Schist of Willow Creek, middle quartzite
Schist of Willow Creek, middle schist
Schist of Willow Creek, lower quartzite
Schist of Willow Creek, lower schist
Daley Creek Quartzite
Robinson Creek Quartzite
Contact, certain
Contact, approximate
Contact, concealed
Normal fault, certain
Normal fault, approximate
Thrust fault, certain
Fault, concealed
Plunging antiform
Plunging synform
Strike and dip of foliation
Lineation showing plunge
Lineation, horizontal
Sample location

◀ **Fig. 2** Geological map of a portion of the northern Albion Mountains. **a** The Mount Harrison Sequence contains the schist of Willow Creek, from which the samples were collected. The field area (*boxed*) is in the hanging wall of the Basin-Elba fault, a major thrust in the hinterland of the Sevier Orogen. **b** Geologic map of the field area located in sections 5, 6, 31, and 32 of the Mount Harrison 7.5-min quadrangle, Cassia County, Idaho. The Daley Creek quartzite, schist of Willow Creek, and Harrison Summit quartzite are overturned. Modified from Miller (1978). Bedding and lineation attitudes were measured in the current study and by Harris (2003)

EKAL16A) show a steep change in almandine (X_{alm}) and grossular (X_{grs}) midway through their core-to-rim profiles corresponding with a textural transition from inclusion-rich cores to inclusion-poor rims. Sample TH203B shows a similar, but less pronounced change, and EKAL29A does not show a discontinuity in chemical zoning or a distinct inclusion texture transition. Mole fraction of pyrope (X_{prp}) generally follows changes in X_{alm}.

With regard to the distribution of Y, two of the garnets have a relatively narrow central Y peak at their cores surrounded by a relatively uniform region of elevated Y concentration (EKAL16A and EKAL29A). Sample TH203B also has a relatively uniform region of elevated Y concentration in the core but appears to lack a central peak, possibly due to sectioning slightly outside of the center of the crystal. The fourth garnet (ALMO13A) does not show an elevated Y concentration in the core, probably due to a cut through the crystal outside of the high-Y core region. Outside of the high-Y region displayed by three of the garnets, the Y concentration decreases outward and then rises sharply to form an annulus. The Y annulus occurs near the inclusion textural transition and the steep change in major-element zoning in three of the garnets, but the location of the annulus is not coincident with those features in all crystals.

Pertinent petrographic and chemical characteristics

The construction of *P–T* paths is aided by petrographic evidence and compositional zoning features: (1) Rare grains of small, ragged staurolite have been observed in three of the four samples (Fig. 6) and are likely present in the fourth (TH203B). (2) Garnet porphyroblasts show

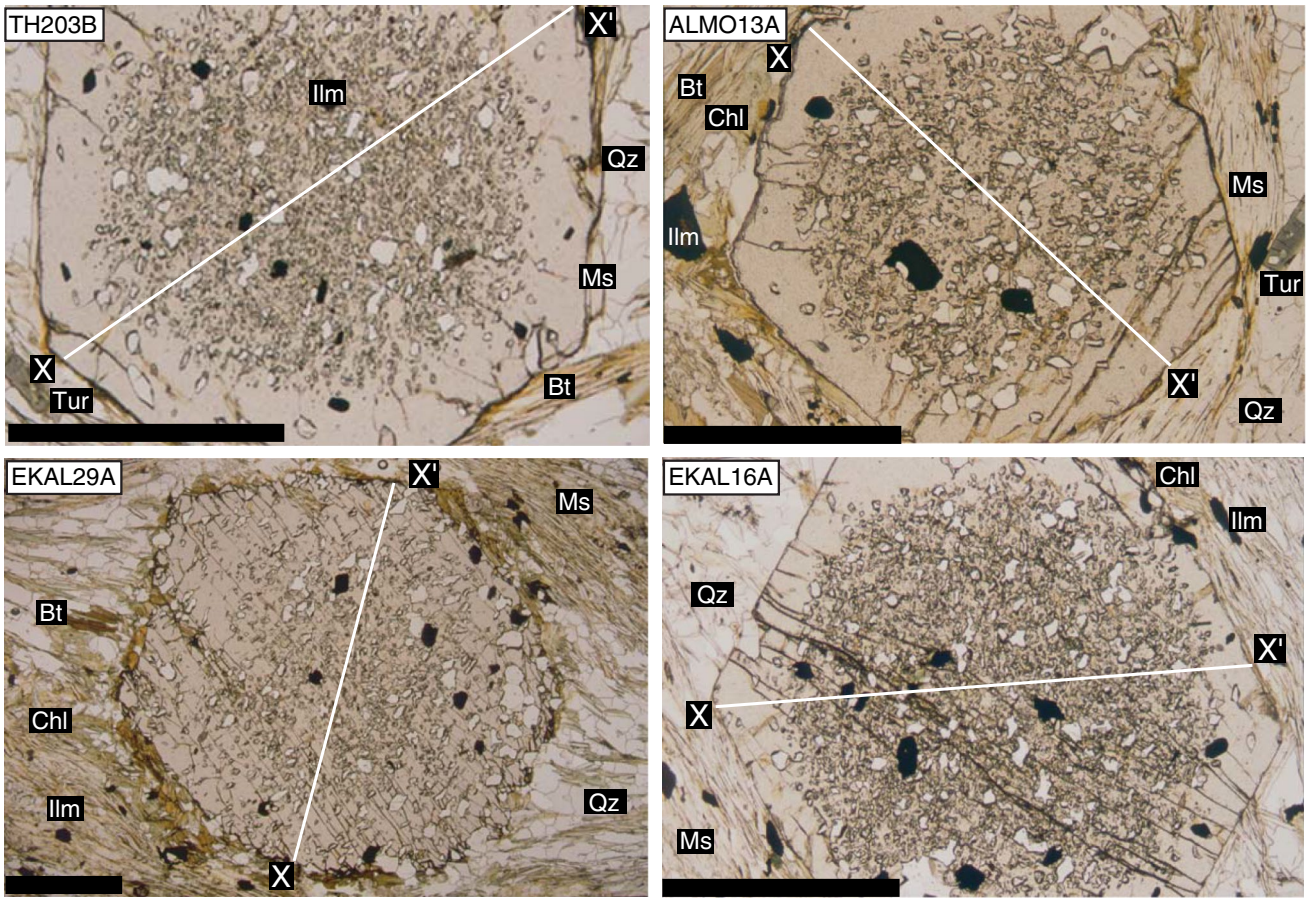

Fig. 3 Photomicrographs of garnet samples in plane-polarized light. Electron microprobe traverses are indicated by lines *X–X′*. Mineral abbreviations after Whitney and Evans (2010): *Bt* biotite, *Chl* chlorite, *Ilm* ilmenite, *Ms* muscovite, *Qz* quartz, *Tur* tourmaline. *Scale bars* are 1 mm

Table 1 Mineral modes

	TH203B			ALMO13A		EKAL16A		EKAL29A		
	X-ray map	Point count	Model input	Point count	Model input	Point count	Model input	X-ray map	Point count	Model input
Qz	36.38	27.64	27.27	44.17	44.44	32.50	31.88	41.32	46.10	35.91
Ms	45.58	53.25	52.67	37.42	37.60	41.25	40.46	34.34	38.00	35.53
Bt	5.66	6.91	6.82	10.43	10.46	1.25	1.23	2.17	10.60	5.49
Grt	(4.92)	4.88	4.84	4.60	3.69	13.75	7.97	(4.71)	4.70	4.65
Chl	4.58	4.88	4.84	1.23	1.21	9.17	8.99	8.13	1.00	8.84
St	0.00	0.41	0.40	0.31	0.30	0.42	0.40	0.11	0.00	0.47
Pl	2.41	0.00	1.98	0.31	2.01	0.00	7.85	8.47	0.30	7.44
Ilm	0.45	1.22	1.19	0.31	0.30	1.25	1.23	0.66	0.30	1.67
Total	99.99	99.19	100.00	98.77	100.00	99.58	100.00	99.90	101.00	100.00

Garnet mode from the X-ray map analysis was assumed the same as determined from point counting because the X-ray map either did not contain garnet or did not cover a large enough thin-section area to accurately represent the garnet mode of the sample

Model input modes were used to calculate initial bulk compositions for *P–T* path modeling

Modes are in volume percent

Mineral abbreviations after Whitney and Evans (2010)

a distinct textural transition between an inclusion-rich core and an inclusion-poor rim (except EKAL29A). (3) In three of the samples, the major-element zoning in garnet changes markedly at the inclusion boundary, whereas EKAL29A displays a smooth zoning profile from core to rim, especially for the ratio of Mg to total Mg + Fe (Mg#). In general, X_{alm} and X_{prp} increase toward the rim, and X_{grs} and X_{sps} decrease; however, along these trends, X_{alm} and X_{grs} show more distinct changes (e.g., X_{grs} increases, decreases, and then increases again from core to rim). (4) Yttrium maps reveal the locations of resorption features in some crystals. All of the garnets have an Y annulus outside of a low-Y trough. In each crystal, the inclusion boundary occurs near the Y annulus, but does not occur at a consistent radius relative to the inclusion boundary: In ALMO13A, the annulus corresponds with the inclusion boundary, but in EKAL16A and TH203B, the annulus appears to lie just outside of the inclusion boundary, and in EKAL29A, the inclusion boundary is absent. These key characteristics act as constraints in the evaluation of the shapes and locations of the *P–T* paths in *P–T* space.

P–T paths

Within the constraints of the observations above, and using the methods described below, a *P–T* path was constructed for each garnet. Recognizing that the rocks share the same *P–T* history, the paths were then aligned with each other through slight adjustments in absolute pressure and temperature (within error) to create a composite *P–T* path.

Fig. 4 Garnet X-ray maps for major and minor elements. Backscattered and secondary electron images are shown to highlight inclusions. *White lines* show the locations of the electron microprobe traverses. *Lighter colors* indicate higher concentrations in the element maps. Element concentration in each map is scaled independently of the others. Matrix is masked in the major-element images to emphasize garnet zoning ▶

Methods

Isochemical phase diagrams

Isochemical phase diagrams were constructed for each sample using the software package THERIAK-DOMINO (de Capitani and Brown 1987; de Capitani and Petrakakis 2010) and the Holland and Powell (1998) database with updates through 2010 and mixing models as described in Online Resource 5. Bulk compositions in the system $MnO–Na_2O–CaO–K_2O–FeO–MgO–Al_2O_3–SiO_2–H_2O–TiO_2$ (MnNCKFMASHT) were calculated from mineral compositions determined by electron probe microanalysis (EPMA) by summing in proportion to mineral modes after converting the modes from volume percent to weight percent. The modes of the phases were determined from point counting with supplemental measurements derived from X-ray maps of portions of the thin sections of samples TH203B and EKAL29A. Plagioclase generally does not show twinning in these rocks and is easily mistaken for quartz in thin section; so the plagioclase modes determined from point counting were assumed to be minimum estimates, and those from X-ray mapping were assumed to be maximum estimates. Thus, the modes of plagioclase in samples ALMO13A and EKAL16A are higher than the

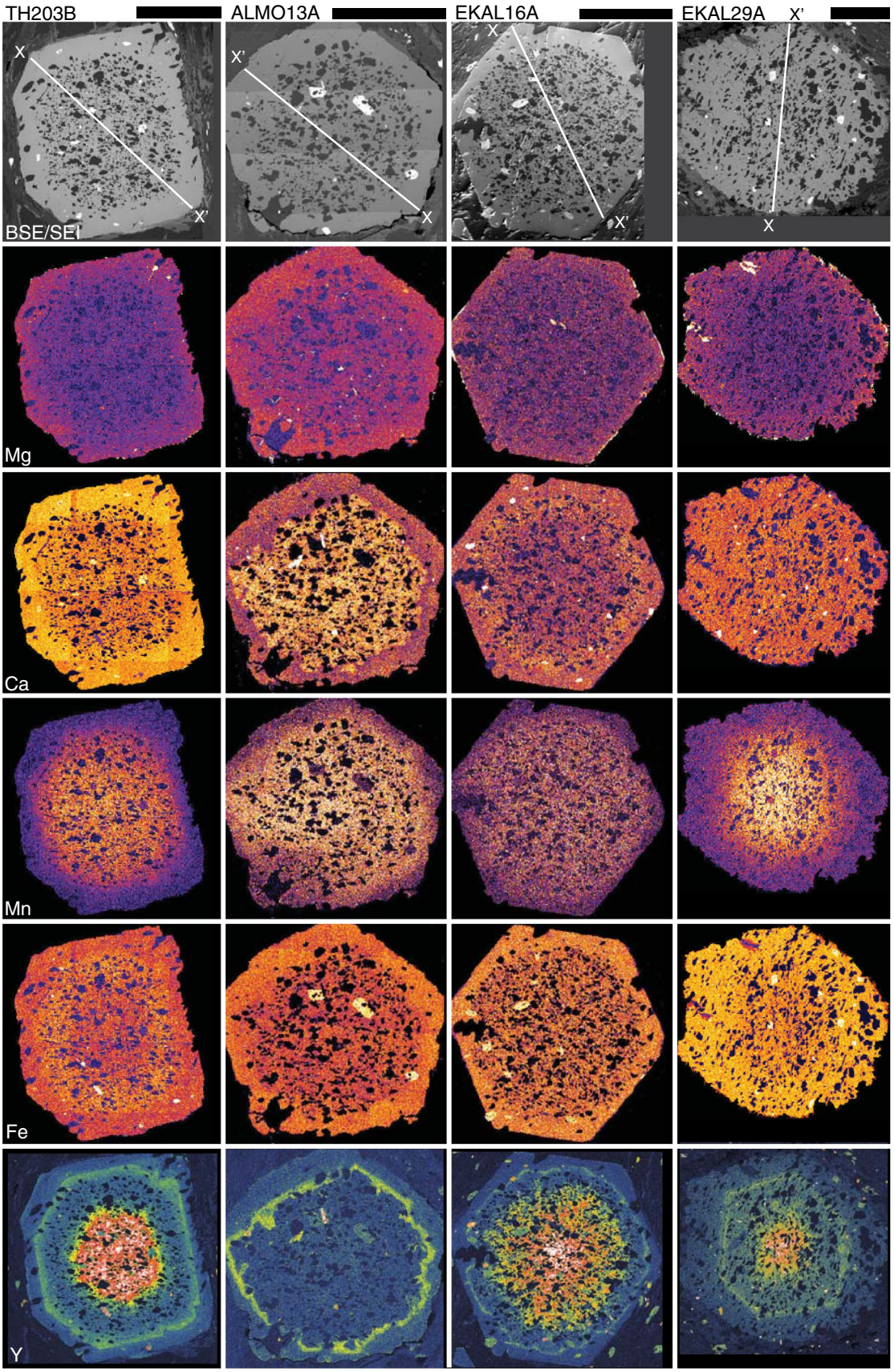
TH203B
ALMO13A
EKAL16A
EKAL29A
X
X'
BSE/SEI
Mg
Ca
Mn
Fe
Y

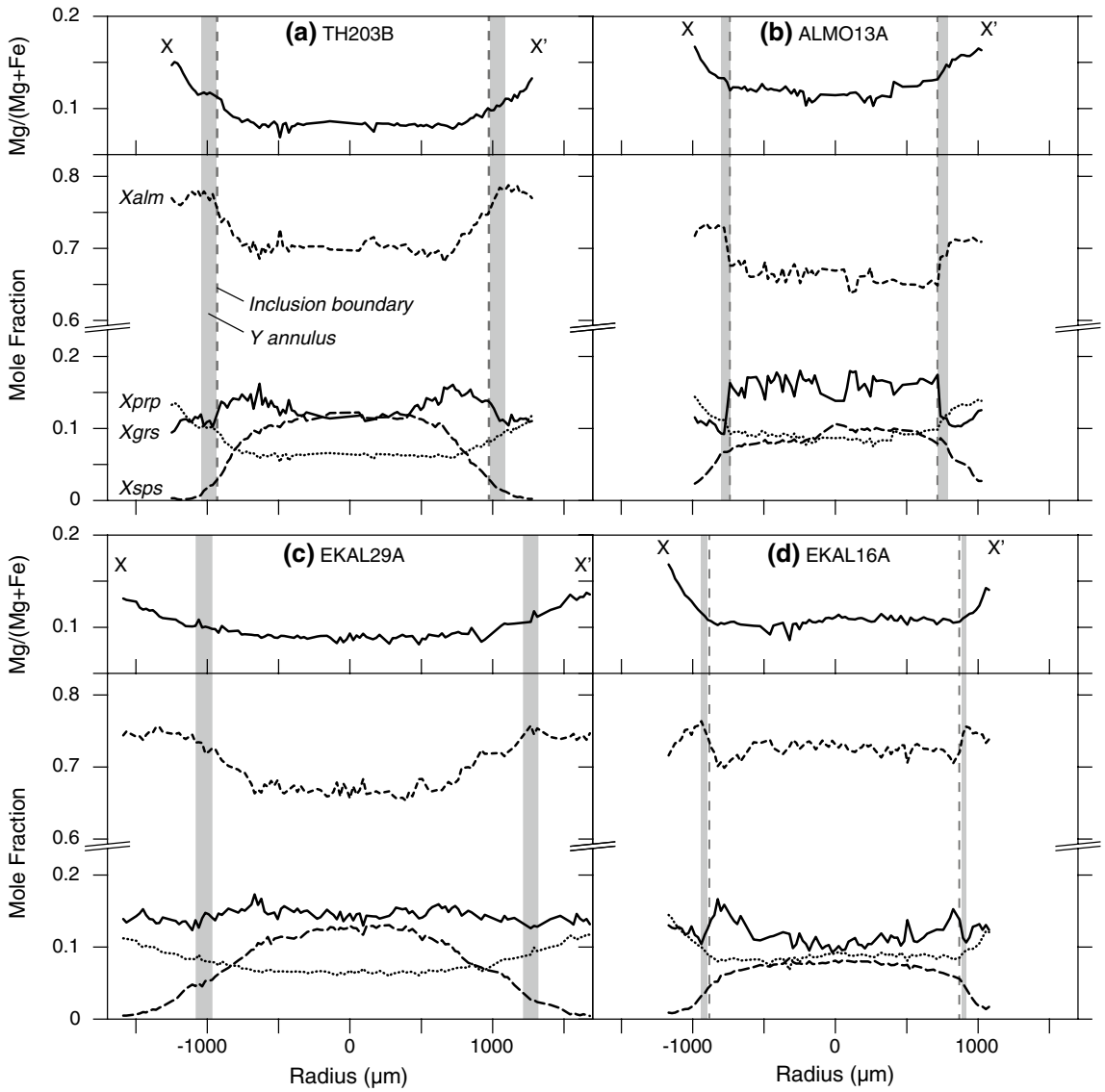

Fig. 5 Garnet major-element concentration profiles. The locations of the inclusion boundaries and the Y annuli were determined from the photomicrographs and element maps. For samples TH203B and EKAL29A, the right side of the traverse was modeled, and for samples ALMO13A and EKAL16A, the left side was modeled

point counting estimates but less than the maximum determined from X-ray mapping (Table 1). Chlorite in sample EKAL29A tends to be proximal to the analyzed garnet, but biotite is observed at greater distances from garnet; so the mode of chlorite was increased, and the mode of biotite was decreased for modeling in order to approximate the volume of rock from which the garnet acquired nutrients.

For the purposes of estimating the contribution of garnet chemical zoning to the bulk composition of each sample, we assumed that all garnet porphyroblasts in the rock are the same size and contain the same chemical zoning. All samples except for EKAL16A have a relatively small garnet mode (<5 %); so the contribution of garnet to the bulk compositions is small, and the possible error associated with assuming a uniform garnet size is negligible (Zuluaga et al. 2005). For EKAL16A, the garnet mode is ~14 %, so there is a possibility of larger errors from our assumption. However, the modeling of all four samples produced consistent results (shown below), so the error introduced to the EKAL16A bulk composition appears to be small. Table 2 shows the bulk compositions used to model each sample, and Fig. 7 shows the resulting isochemical phase diagrams and locations of core garnet isopleths.

Garnet zoning and P–T path modeling

Using the bulk compositions and garnet zoning data from each sample, the automated routine of Moynihan

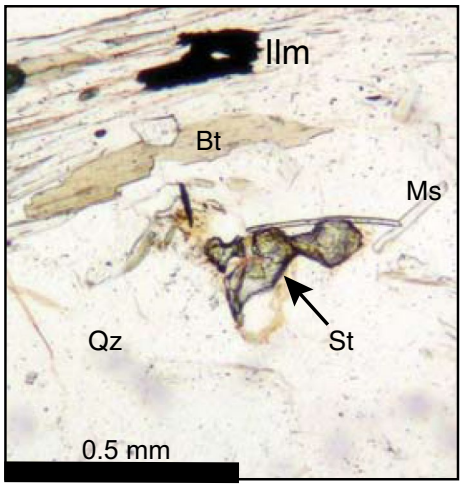

Fig. 6 Photomicrograph of staurolite in plane-polarized light. Rare staurolite grains are ragged and small. Mineral abbreviations after Whitney and Evans (2010): *Bt* biotite, *Ilm* ilmenite, *Ms* muscovite, *Qz* quartz, *St* staurolite

Table 2 Input for *P–T* path modeling

	TH203B	ALMO13A	EKAL16A	EKAL29A
T (°C)	500	475	515	465
P (bars)	4275	4750	4350	3500
Na	2.25	1.79	2.66	2.28
Mg	2.39	2.54	2.20	2.62
Al	24.64	19.28	22.39	20.37
Si	50.15	60.31	54.12	55.89
K	6.13	5.13	4.38	4.76
Ca	0.39	0.33	0.86	0.63
Ti	0.82	0.37	0.78	1.11
Mn	0.14	0.10	0.19	0.13
Fe	4.35	3.47	5.04	5.05

Compositions are in mole percent

Excess H and stoichiometric O were used in all models

and Pattison (2013a, hereafter referred to as MP13) was employed to construct the *P–T* paths. The MP13 script runs in MATLAB and calls THERIAK-DOMINO to calculate an isochemical phase diagram starting with our estimate of the bulk composition of the rock and a *P–T* point outside of the garnet stability field. The MP13 script uses an optimization function in MATLAB to search the *P–T* grid for the smallest misfit between a modeled garnet core composition and the measured core composition (the intersection of garnet compositional isopleths) and then calculates the portion of the bulk composition that is sequestered in the newly formed garnet. The components sequestered in the garnet are subtracted from the bulk composition to estimate an effective bulk composition for the next step of garnet growth. A new isochemical phase diagram is calculated from the effective bulk composition, and the process is repeated for all steps along one half of the garnet zoning profile from core to rim. The steps correspond to microprobe analyses except where inclusions or cracks prevented analysis. In these gaps, the garnet compositions were interpolated to maintain small and consistent spacing between points. For each step, the intersection of garnet compositional isopleths yields an estimate of the *P–T* conditions of incremental garnet growth, culminating in a *P–T* path (Online Resources 1–4, 6).

Results of modeling

As shown in Fig. 8, the simulated major-element garnet zoning profile for sample TH203B fits the observed zoning very well for all four components. For the remaining three samples, X_{grs} and X_{sps} fit well, whereas X_{alm} and X_{prp} are relatively more offset from the observed profiles. In all samples, the values of Mg# are consistently lower than the observed values with the largest difference displayed in samples ALMO13A and EKAL16A. The differences between the simulated and observed zoning profiles are reflected in the locations of the *P–T* points determined by the MP13 routine relative to the isopleths (e.g., Fig. 9). Each point plots near the intersection of X_{grs} and X_{sps} and midway between X_{alm} and X_{prp}.

Three distinct segments in the *P–T* path are revealed from the model of sample TH203B (Fig. 9): The first segment (*I*), from step one to step 41, shows an approximately isothermal increase in pressure followed by an increase in pressure and temperature. The second segment (*II*), from step 41 to step 50, follows a trend of decreasing pressure and increasing temperature. The third segment (*III*), from step 50 to step 77, is a nearly isothermal increase in pressure. The paths from the remaining samples (Fig. 10) exhibit all or some of the segments captured in sample TH203B. Sample EKAL16A yields a path that appears to contain all three of the major segments of the TH203B path, although the segments have steeper trends in *P–T* space due to mismatched model X_{alm} and X_{prp} slopes that reduce the magnitude of temperature change from core to rim. In sample ALMO13A, which lacks high-Y concentration in the center of the crystal section, only a small portion of Segment *I* and the latter segments of the path are recorded, consistent with a rim-ward cut section that only contains zoning from the outer core through the rim of the garnet. Sample EKAL29A yields a path that does not show a decrease in pressure midway through garnet growth, so this sample could contain only Segments *I* and *III* with Segment *II* missing, or the entire modeled path is either Segment *I* or *III*. In the next section, we consider additional observations to make slight adjustments to the placement of the paths in *P–T* space, so that similar segments are aligned, to produce a composite path.

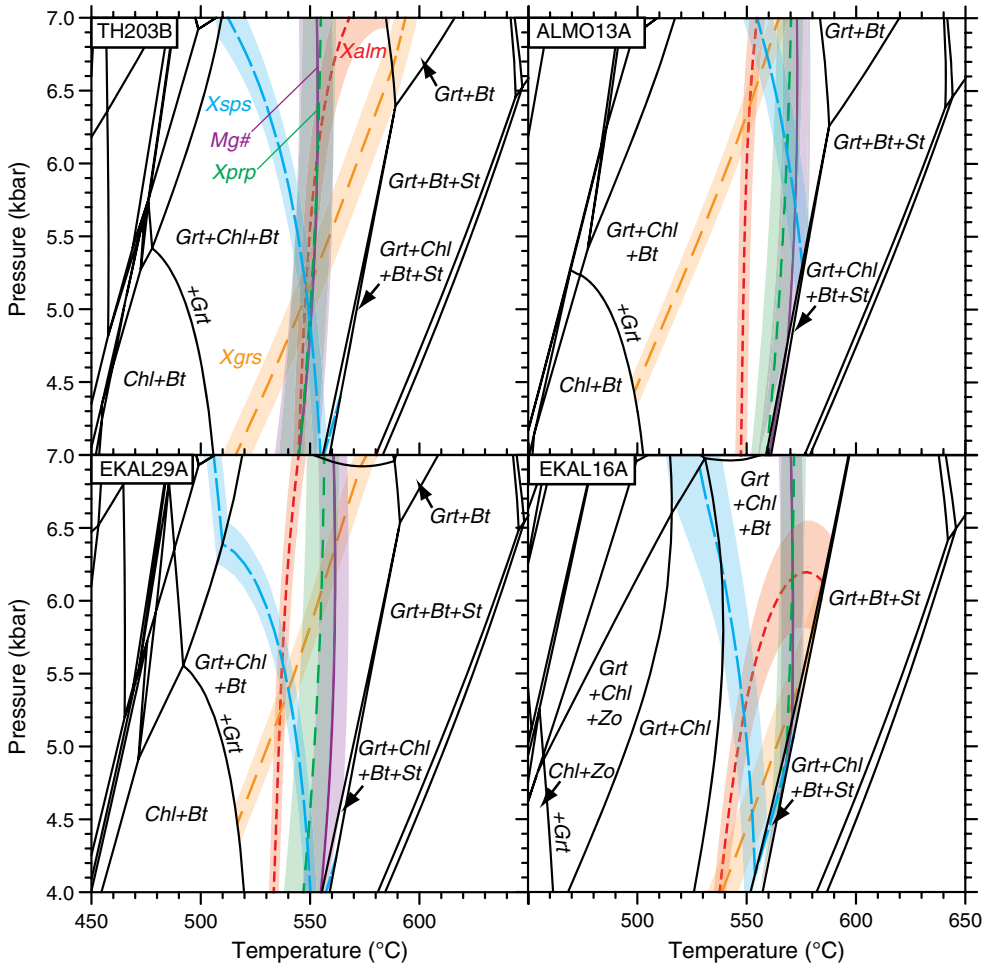

Fig. 7 Isochemical phase diagrams for whole-rock bulk compositions of all samples. Diagrams were constructed within the chemical system MnNCKFMASHT, and all labeled assemblages include muscovite, quartz, plagioclase, ilmenite, and H_2O. Mineral abbreviations after Whitney and Evans (2010): *Bt* biotite, *Chl* chlorite, *Grt* garnet, *St* staurolite, *Zo* zoisite. Measured garnet core isopleths are shown for Mg# and mole fraction of almandine (X_{alm}), pyrope (X_{prp}), grossular (X_{grs}), and spessartine (X_{sps}) with *shading* that spans two contour intervals of 0.01 mol fraction. Assuming the same span of contour intervals for all four isopleths provides a basis for determining the relative sensitivity of each. Narrower isopleth fields suggest tighter constraints. For clarity, isopleths are not plotted at higher temperature than the staurolite isograd

Discussion: *P–T* path construction

We use the following observations and considerations to help position the *P–T* path segments relative to reactions on the phase diagrams: (1) inclusion textural boundaries, (2) Y zoning characteristics that suggest garnet resorption, (3) the presence of staurolite in most samples, and (4) uncertainties in the isochemical phase diagrams.

Inclusion texture

We interpret the change in the internal crystal texture from inclusion-rich (quartz-bearing) to inclusion-poor to reflect a change in the garnet growth reaction from one that produces quartz to one that consumes it (e.g., Farber et al. 2014). Isopleths of quartz mode on isochemical plots show that this change occurs across the staurolite-in reaction for rocks following a *P–T* path similar to the one determined for this study (Fig. 11). Along a prograde *P–T* path (Fig. 11, "Simple Path"), a pelitic bulk composition similar to our samples will experience garnet growth with increasing quartz mode at lower temperatures than the staurolite-in reaction and decreasing quartz mode at higher temperatures than the reaction. Thus, garnet growing at temperatures below the staurolite isograd is likely to occlude quartz grains (although in the immediate presence of garnet, quartz may be partially dissolved to supply some SiO_2 to garnet). In contrast, because quartz is a reactant at temperatures higher than the staurolite isograd, it is more likely to be fully consumed as the growing garnet surface approaches.

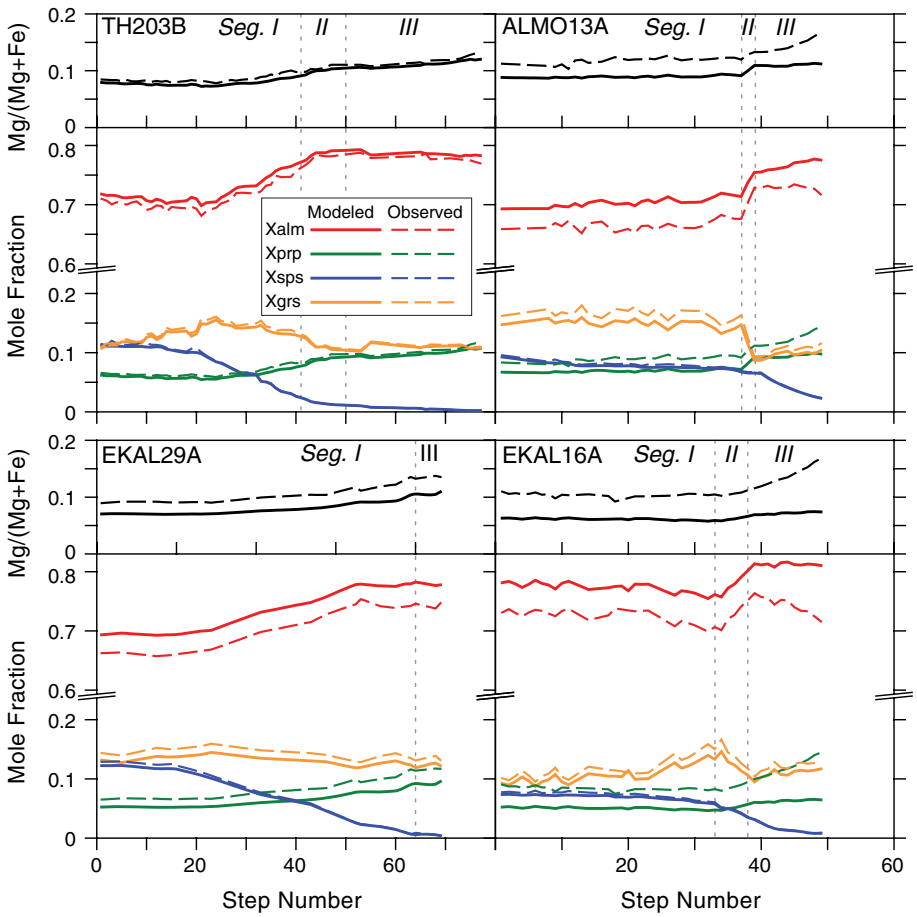

Fig. 8 Modeled garnet chemical zoning compared with measured zoning profiles. One side of each garnet profile was simulated from core to rim. Zoning from samples ALMO13A and EKAL16A have been reflected across a vertical axis to orient all profiles with their rims to the right side of figure. *Dashed vertical lines* mark the boundaries between segments of the *P–T* path (e.g., Fig. 9)

A similar effect on quartz inclusions is expected for a more complex path (Fig. 11, "N Path"). A garnet growing along *P–T* path Segments *I* and *IIa* should be accompanied by the net production of quartz in the rock and the incorporation of quartz inclusions. Along Segments *IIb* and *III*, however, the garnet is either not growing (*IIb*) or follows decreasing quartz mode (*III*) and should result in inclusion-free garnet growth. If this model is correct, the dramatic change in quartz inclusion density marks the crossing of the staurolite-in reaction and suggests that the rim segments of the garnets grew inside the staurolite field (e.g., Farber et al. 2014). Furthermore, the garnets are likely to have experienced a small amount of resorption along Segment *IIb* during staurolite growth (e.g., Florence and Spear 1993; Pyle and Spear 1999; Farber et al. 2014; Cruz-Uribe et al. 2015). Three of the four garnets analyzed in this study display the change in quartz inclusion density from core to rim. The one that does not, sample EKAL29A, does not have an inclusion-poor rim, possibly suggesting that the staurolite isograd is located at slighter higher temperature for the bulk composition of this sample and that the entire garnet grew in the chlorite-bearing field.

Yttrium zoning

In our samples, the Y zoning in garnet provides evidence of whether thin-section cuts passed through the center of the crystals and whether apparent resorption took place in some crystals. Three of the samples (EKAL16A, EKAL29A, and TH203B) show, from core to rim, a plateau in Y concentration, a decrease in Y concentration, and a rise in Y concentration in the form of an annulus. The fourth sample (ALMO13A) shows only an Y annulus.

Garnet crystals in pelitic rocks commonly have high-Y concentrations in their cores and lower concentrations in their rims, sometimes seen as an Y peak at the core and a smooth decrease in Y toward the rim (e.g., Hickmott et al. 1987; Pyle and Spear 1999; Skora et al. 2006; Moore et al. 2013). In some cases, garnets may show a central plateau or an Y annulus (Pyle and Spear 1999). These features can be used to infer the location of the thin-section cut through the crystal. Sample EKAL16A (and possibly TH203B) appears to show the full extent of the *P–T* path due to sectioning near the center of the crystal, indicated by the central Y peak. The modeled *P–T* paths of TH203B and EKAL16A show a longer history of

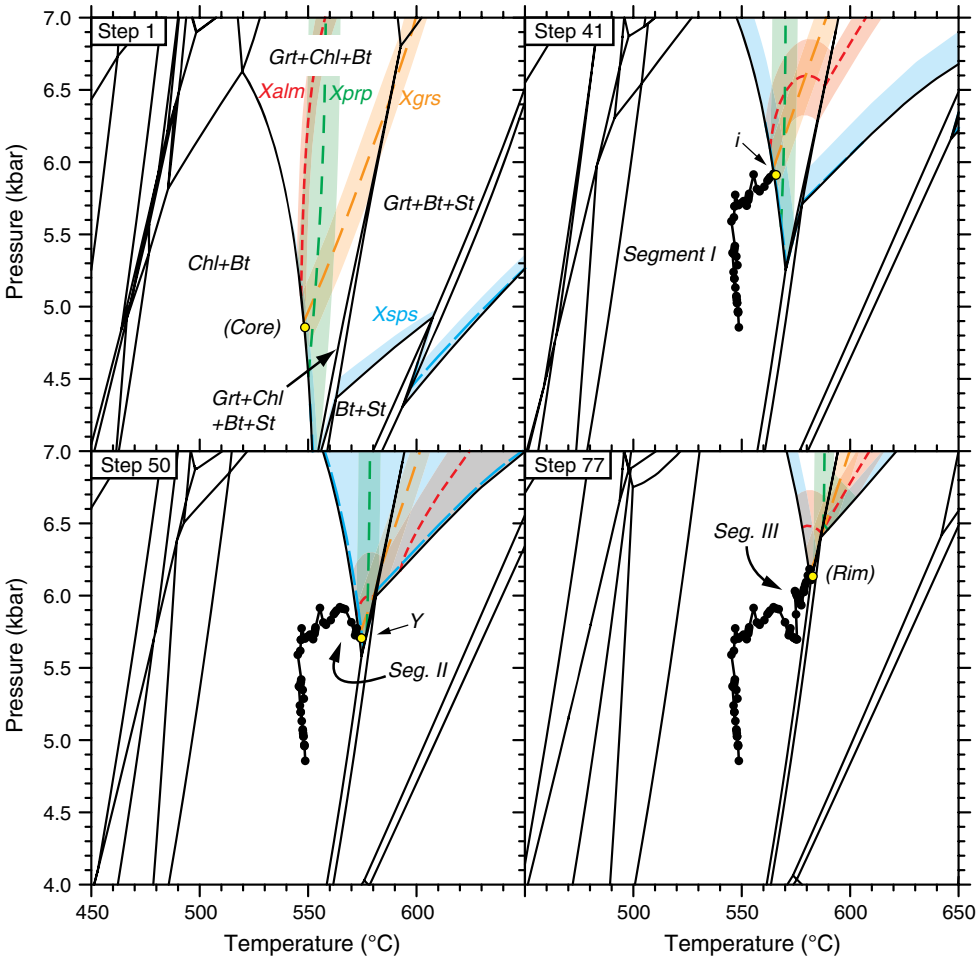

Fig. 9 Isochemical phase diagrams for sample TH203B. The development of the path is illustrated with progressive adjustments to the effective bulk composition from modeling step 1 through the final step (77). Diagram construction and labeling follows that of Fig. 7. The locations of the inclusion boundary (*i*) and the outer edge of the Y annulus (*Y*) are shown. Portions of the *P–T* path that are consistent with the hypothesized path segments in the text are labeled (*I–III*)

P–T changes relative to the other two samples, supporting the notion that these garnets were sectioned close to their cores. Sample ALMO13A lacks high-Y concentrations in the center, suggesting that the crystal was not cut through the center, and the *P–T* path generated from this crystal lacks the early portion of the *P–T* path, confirming that the difference in Y zoning is a result of sectioning rather than differences in garnet growth conditions or significant differences in rock bulk composition.

A common mechanism used to explain Y annuli in garnet in a pelitic rock is the breakdown of Y-bearing accessory phases like xenotime during garnet growth (Pyle and Spear 1999; Spear and Pyle 2010). Figure 12 shows a schematic xenotime zero-mode line after Spear and Pyle (2010) with an overlay of the hypothesized "N Path" from Fig. 11. Our bulk compositions and mineral suites (including monazite) are typical of pelitic rocks and likely fall within the range described by Spear and Pyle (2010). Thus, the schematic xenotime zero-mode line may explain how observed Y zoning patterns developed along the *P–T* path determined in this study. Keeping in mind that garnet only grows along Segments *I* and *III*, if garnet growth first occurred during the progressive dissolution of xenotime early along Segment *I*, the Y concentration would have been buffered and the Y zoning profile would develop a plateau like in sample TH203B. After xenotime was fully consumed (along Segment *I*), the garnet would record a low-Y concentration in its outer core. If the rock returned to the xenotime stability field (Segment *IIb*), xenotime could become stable again. A rise in pressure at the start of Segment *III* would consume the xenotime again, producing an Y annulus in garnet. Because each of our samples exhibits unique Y annulus locations relative to the inclusion boundary, the locations of the stability fields associated with each rock were probably slightly different, and each rock crossed into and out of the xenotime field at different points along the *P–T* path. Sample EKAL29A is somewhat unique among our samples but could have crossed into the staurolite field briefly, and then, depending on the orientations of the mineral stability curves and the *P–T* path (staurolite-in reaction line is shallow relative to Segment *III*), crossed back into the chlorite-bearing field.

The Y annulus in sample ALMO13A is especially revealing because it has an irregular and embayed

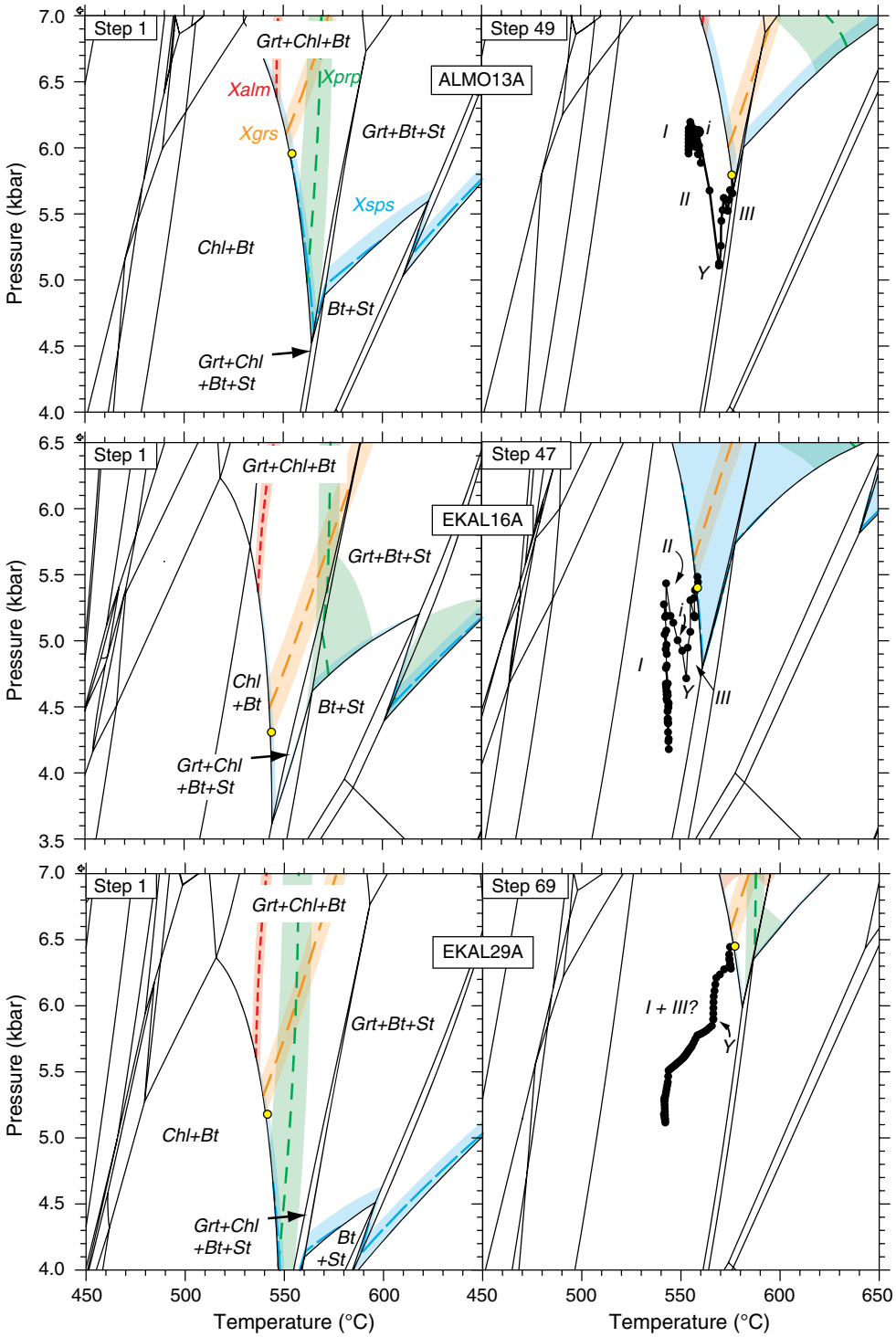

Fig. 10 Isochemical phase diagrams for sample ALMO13A, EKAL16A, and EKAL29A. The development of each path is illustrated using modeling step 1 and the final step for each sample. Diagram construction and labeling follow that of Figs. 7 and 9

appearance (Fig. 4). We interpret this feature as the boundary between early growth of the garnet core and later growth of the garnet rim, with the irregular boundary highlighting the partially consumed rim of the earlier garnet crystal (e.g., Zeh and Millar 2001). Sample EKAL16A also shows an irregular Y annulus, suggesting that this crystal may have experienced a small amount of resorption as well. Sample TH203B has an annulus with a gradual rise in concentration toward the rim and a relatively sharp outer boundary; yet, three visible embayments are highlighted by the annulus at locations aligned with the corners of the crystal. However, given that the inclusion boundary is closer to the interior rather than the exterior of the annulus in this crystal, we suggest that

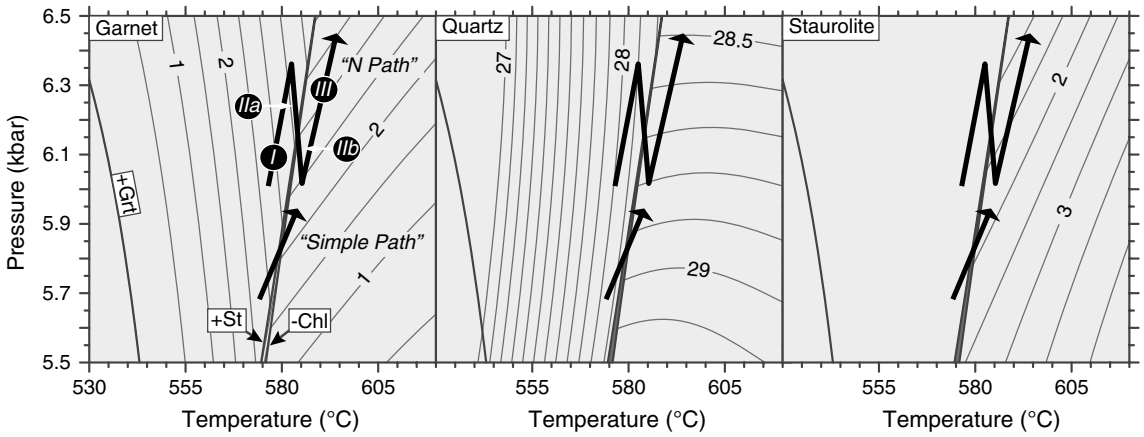

Fig. 11 Mode contours for garnet, quartz, and staurolite with hypothetical *P–T* path. The first or last appearance of indicated phases is shown (e.g., +Grt, −Chl) along with mode values (volume %) for a portion of the TH203B model. "N Path" is labeled with segment numbers described in the text

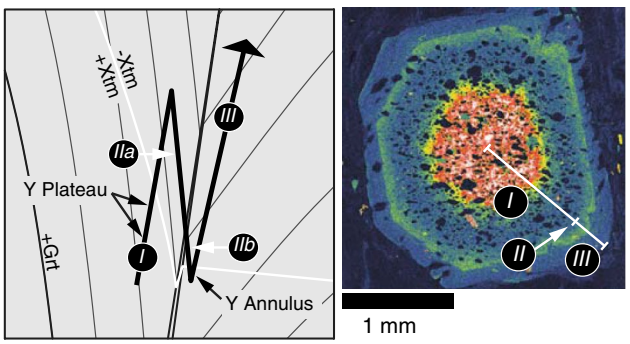

Fig. 12 Schematic xenotime zero-mode line with hypothetical *P–T* path overlay. While following the *P–T* path, if the rock exits and then reenters the xenotime stability field, the observed Y zoning profile in our samples could result (see text for discussion). Note that garnet growth only occurs along Segments *I* and *III*. The xenotime zero-mode line is based on Spear and Pyle (2010). An Y map from sample TH203B is shown as an example. *Lighter colors* indicate higher concentrations of Y

resorption probably occurred before the annulus formed, and therefore, evidence of the resorption event is not visible in the annulus.

Presence of staurolite

Several of the samples contain small, ragged staurolite grains (Fig. 6), suggesting that they passed through the staurolite field. The orientation of the *P–T* path in the staurolite field plays a role in whether or not staurolite grows or dissolves. In Fig. 11, along Segment *IIb* of "N Path," garnet mode decreases and staurolite mode increases. This segment could be responsible for growth of a small amount of staurolite. Further along the path (Segment *III*), garnet mode will increase, while staurolite dissolves, potentially leaving the small, ragged grains observed in our thin sections.

Evidence of uncertainty in isochemical phase diagrams

Sources of uncertainties in isochemical phase diagrams include bulk composition estimates, thermodynamic data, and activity models (Powell and Holland 2008). In addition, the effects of disequilibrium in the form of thermal overstepping should be considered (Pattison and Tinkham 2009; Carlson 2011; Pattison et al. 2011; Kelly et al. 2013; Spear et al. 2014; Carlson et al. 2015). Methods involving equilibrium modeling and isochemical phase diagram interpretations carry uncertainties that derive from the fact that crystallization likely began after thermal overstepping, i.e., nucleation of product crystals at higher temperatures than predicted by the calculated equilibrium reaction (e.g., Rubie 1998; Waters and Lovegrove 2002; Zeh and Holness 2003; Pattison and Tinkham 2009; Ague and Carlson 2013; Kelly et al. 2013) as indicated by the rarity of garnet core isopleths intersecting along the garnet zero-mode line on an isochemical phase diagram (e.g., Stowell and Tinkham 2003; Zeh et al. 2005; Dragovic et al. 2012; Berg et al. 2013; Spear et al. 2014). Even in the study by Berg et al. (2013), in which most sources of error were minimized greatly, garnet core isopleths intersected at higher temperatures than the zero-mode line by as much as 30–100 °C. Likewise, isopleth intersections for garnet nucleation conditions in our samples occurred at temperatures higher than the garnet zero-mode line (Fig. 7). For our best-fit sample (TH203B), the difference in the equilibrium temperature and the isopleth intersection represents approximately 50 °C of thermal overstepping. Spear et al. (2014) suggest that even isopleth intersections may underestimate garnet growth conditions. Nonetheless, we consider that differences in garnet composition along chemical zoning profiles should still provide a reliable basis for determining *P–T* path shapes from thermodynamic calculations (Kohn

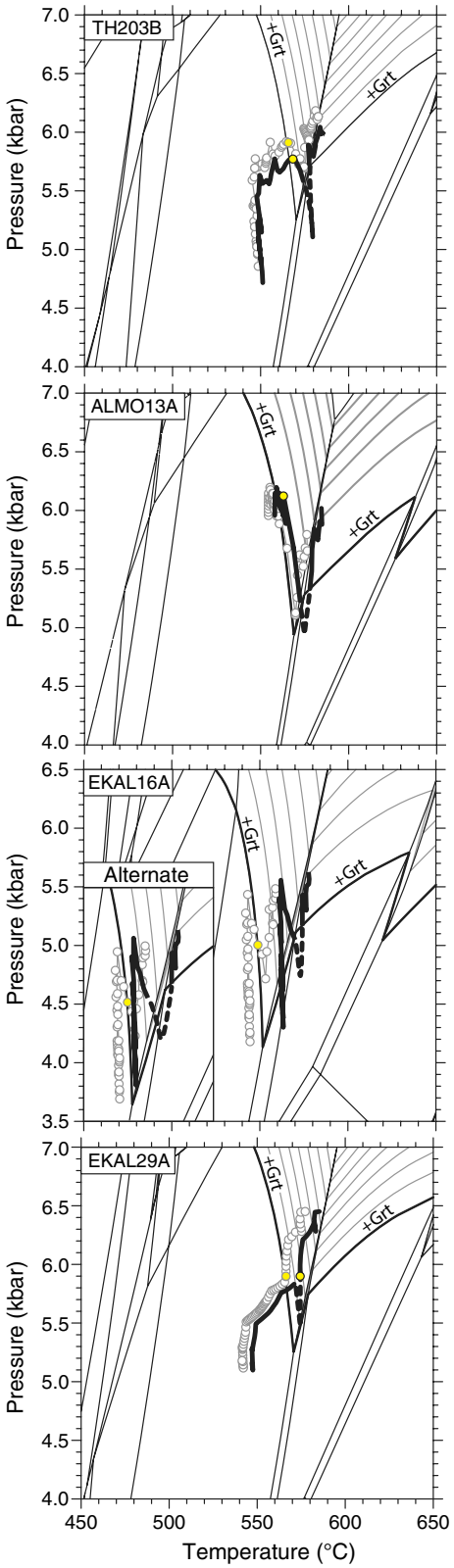

Fig. 13 Modeled *P–T* paths shifted in pressure and temperature to conform to petrographic and chemical evidence. Paths shown with *white dots* are those that result directly from the modeling. *Thick black lines* represent the shifted paths. *Dashed portions* of the paths indicate missing portions of the paths that are inferred to have been lost during resorption of garnet. An alternate interpretation of sample EKAL16A produces a path with a larger temperature range. Diagram construction and labeling follows that of Figs. 7 and 9

1993), with overstepping contributing mainly to uncertainty in the absolute location of the paths in *P–T* space.

Comparison of the modeled Mg# and the measured values shows that the modeled values tend to be lower than those measured in the natural samples (Fig. 8). Considering the temperatures of crystallization, which are less than about 600 °C, and a reasonable duration of crystallization of less than 20 Myr (Hoisch et al. 2008), the length scales of diffusion of Fe and Mg are likely to be small, in the order of 40–50 μm (Carlson 2006; Caddick et al. 2010). Thus, the Mg# measured in these samples should be well preserved, and the difference from the modeled value may indicate that the isopleth intersections located by the automated routine represent underestimated temperatures. We propose that this may be due to inaccuracies in bulk composition estimates, garnet activity models, thermodynamic data, or effects of disequilibrium. Depending on the magnitude of the Mg# misfit, which is smallest in TH203B and largest in EKAL16A, shifting the paths to higher temperatures by 5–20 °C causes the paths to align with mineral assemblage fields and reactions in such a way as to permit a simple interpretation that satisfies the textural, mineralogical, and chemical constraints described previously (and further discussed in the next section). The shifts in temperature are well within uncertainties predicted for thermobarometry (Kohn and Spear 1991; Todd 1998; Powell and Holland 2008), and because the shape of each path is based on differential garnet compositions, the shape should be robust compared to its absolute placement in *P–T* space (Kohn 1993).

P–T path correlations

The relatively close fit of the model to the observed zoning for TH203B justifies the use of this model as a starting point for construction of a composite path. This model appears to encompass the changes in *P–T* conditions experienced by all of the garnet crystals we studied. The loss of quartz inclusions and the change in major-element zoning from core to rim suggest that the path crossed the St-in reaction. To align this point in the path with the St-in reaction requires a shift to higher temperatures of <20 °C and an increase in pressure of <500 bars. Figure 13 shows the paths after they have been shifted.

Three of the paths (TH203B, ALMO13A, EKAL16A) were shifted so that they account for the observed hiatus in the correct locations in the garnet profiles. Growth of the inclusion-rich cores (Segment *I*) took place during increasing pressure. The path then decreased in pressure, approximately following a garnet mode contour (hiatus in growth along

Segment *II*), then crossed the staurolite-in reaction, causing resorption to take place (Segment *IIb*). Growth of the garnet resumed in the staurolite field with increasing pressure to form the rim (Segment *III*). Three of the samples fit this interpretation well. However, sample EKAL29A lacks some characteristics that were found in other samples: no loss of quartz inclusions in the rim, no decrease in pressure along the model *P–T* path, and no abrupt changes in major-element zoning. A plausible explanation is that EKAL29A experienced *P–T* changes that followed the garnet mode contour (hiatus) during Segment *IIa* and did not cross into the staurolite field (no consumption) along Segment *IIb*. If this was the case, evidence of the path along Segment *II* would not be recorded. When rim growth resumed, the garnet was on the low-temperature side of the staurolite-in reaction and grew with quartz as a product of the reaction making abundant inclusions in the rim. A difference in the bulk composition of sample EKAL29A compared to the other samples could account for rim growth on the low-temperature side of the staurolite isograd.

Taking all of the shifted versions of the paths together, an overall composite path was constructed (Fig. 14a). While constructing the overall path, it became apparent that the misfit of X_{alm} and X_{prp} in the model of sample EKAL16A produced a path that spanned too narrow of a temperature range to maintain consistency with the other samples. To simulate the effect of a better fit to X_{alm} and X_{prp}, we shifted the core portion of the path (low-*T* side of St-in reaction) about 10 degrees lower in temperature and kept the rim portion at higher temperature, producing an effectively larger temperature range, which is the case in the well-fit samples (TH203B and EKAL29A). The path is shown in the inset of Fig. 13 (EKAL16A Alternate) and used in the composite path construction in Fig. 14.

Putting all of the characteristics together, the path shown in Fig. 14b describes the preferred garnet growth history: (*I*) growth of the garnet core occurred at lower temperature than the staurolite-in reaction where quartz is a product of the reaction; (*IIa*) garnet growth paused (hiatus) as pressure decreased and the path followed the garnet mode contour; (*IIb*) partial consumption occurred during the decrease in pressure by one or more possible reactions: a reaction involving the loss of chlorite at the staurolite isograd, or a reaction that consumes garnet and grows staurolite with decreasing pressure in the staurolite field; (*III*) growth of the garnet rim occurred inside the staurolite field where quartz is a reactant (growth of the rim of sample EKAL29A occurred inside the chlorite field where quartz remained a product of the reaction). Note that the garnet zero-mode line migrates to lower temperatures and pressures when garnet is partially consumed. Therefore, the precise location

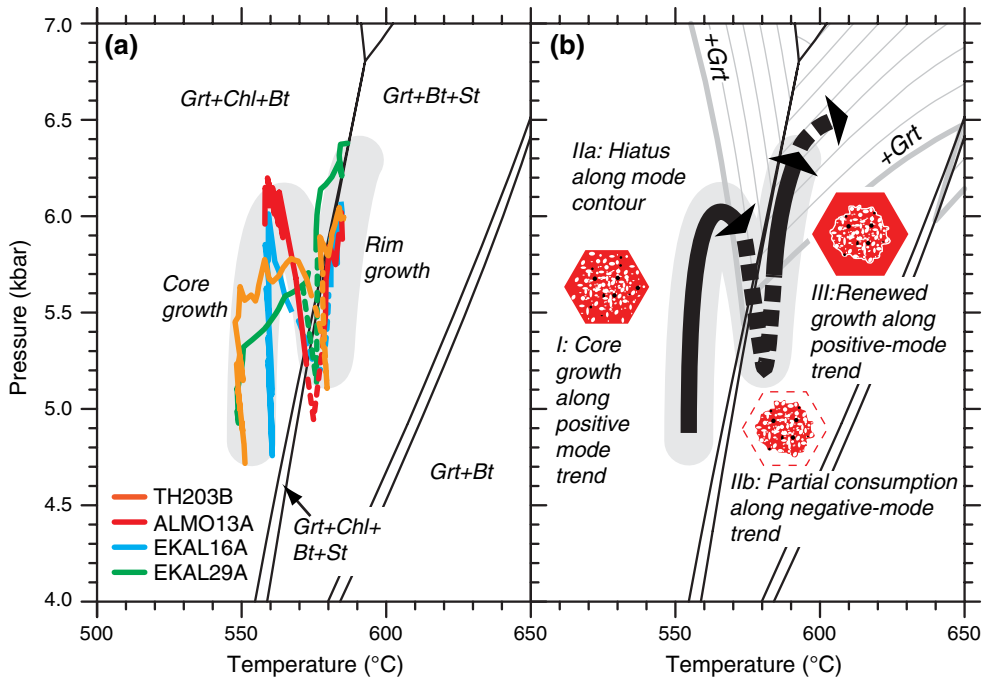

Fig. 14 Composite *P–T* path and interpretation. **a** Starting with the shifted version of path TH203B, all of the paths are aligned to describe the "average" changes in *P–T* (gray swath) experienced in the hanging wall of the Basin-Elba fault. **b** The petrographic, chemical, and modeling evidence is interpreted as an "N shaped" *P–T* path that produced the illustrated garnet features for three of the four samples following the segments of the hypothesized *P–T* path. Sample EKAL29A differs in that it likely experienced rim growth (Segment *III*) in the chlorite-bearing field just down temperature of the staurolite isograd. All labeled assemblages include muscovite, quartz, plagioclase, ilmenite, and H_2O. Mineral abbreviations after Whitney and Evans (2010): *Bt* biotite, *Chl* chlorite, *Grt* garnet, *St* staurolite

Table 3 Lu–Hf isotope data for the schist of Willow Creek, northern Albion Mountains

Sample	Lu (ppm)[a]	Hf (ppm)[a]	$^{176}Lu/^{177}Hf$[b]	$^{176}Hf/^{177}Hf$[c,d]	Grt–WR ages (Ma)[e]	Error (2σ Ma)
MW07AL-1						
G1	3.18	0.113	4.002	0.292206 ± 39	132.6	1.0
G2	3.35	0.238	2.003	0.287180 ± 33	130.3	1.6
G3	3.47	0.364	1.354	0.285644 ± 32	132.7	2.5
G4	2.03	0.154	2.898	0.289342 ± 32	130.0	1.2
WRS	0.551	0.218	0.3581	0.283170 ± 32		
WRB	0.927	8.21	0.0160	0.282289 ± 29		
MW02AL-1a						
G1	6.85	0.126	7.755	0.302936 ± 31	141.8	0.8
G2	5.57	0.083	9.608	0.307156 ± 33	137.9	0.7
G3	6.94	0.112	8.849	0.305162 ± 34	137.7	0.7
G4	7.06	0.178	5.637	0.297205 ± 32	140.7	0.8
G5	7.01	0.153	6.516	0.299163 ± 32	137.8	0.8
WRB1	0.577	6.16	0.0133	0.282168 ± 28		
WRB2	0.505	5.54	0.0129	0.282177 ± 28		
WRS1	0.356	0.121	0.4193	0.283440 ± 29		
WRS2	0.566	0.367	0.2193	0.282959 ± 29		

[a] Lu and Hf concentrations determined by isotope dilution with uncertainties estimated to be better than 0.5 %

[b] Uncertainties for $^{176}Lu/^{177}Hf$ for the purpose of regressions and age calculations are estimated to be 1.0 % based on duplicate analysis of rock standards (Vervoort et al. 2004; Cheng et al. 2008)

[c] $^{176}Hf/^{177}Hf$ ratios were corrected for instrumental mass bias using $^{179}Hf/^{177}Hf = 0.7935$ and normalized relative to $^{176}Hf/^{177}Hf = 0.282160$ for JMC-475 (Vervoort and Blichert-Toft 1999). Epsilon Hf values calculated with Lu–Hf CHUR values of Bouvier et al. (2008) and the ^{176}Lu decay constant value of Scherer et al. (2001) and Söderlund et al. (2004)

[d] Reported errors on $^{176}Hf/^{177}Hf$ represent within-run uncertainty expressed as 2σ, standard error. Estimated total uncertainty on individual $^{176}Hf/^{177}Hf$ measurements is 0.01 % or about 1 ε_{Hf} unit. These are added to the within-run uncertainties in quadrature for the purpose of regressions and age calculations

[e] Garnet–whole-rock isochron ages reported for each garnet fraction using the $^{176}Hf/^{177}Hf$ and $^{176}Lu/^{177}Hf$ ratios for the garnet fraction combined with the $^{176}Hf/^{177}Hf$ and $^{176}Lu/^{177}Hf$ ratios from the Savillex whole-rock analysis

at which the rim began regrowth is unknown but probably close to the conditions determined from modeling.

Lu–Hf garnet geochronology

Two samples of the schist of Willow Creek were analyzed for garnet geochronology by the Lu–Hf method (Anczkiewicz et al. 2007; Cheng et al. 2008): samples MW07AL-1 and MW02AL-1a. Sample MW07AL-1 is of a similar bulk composition to the pelitic schist analyzed in this study, whereas sample MW02AL-1a is from a more Al-rich bulk composition. The two samples differ primarily in the amount of staurolite present; MW07AL-1 contains less than 1 % staurolite as very small anhedral grains, whereas MW02AL-1a contains abundant staurolite (~10 %) as large idioblastic grains. The garnet crystals in both samples have core-rim structures similar to those analyzed in this study for *P–T* paths. Consequently, we interpret the garnets in both dated samples to have grown concurrently and as a result of the same reaction history as the garnets for which *P–T* paths were determined in this study. The analyses were performed at Washington State University using the methods described in Cheng et al. (2008). Analytical results are shown in Table 3, and isochron plots are shown in Fig. 15.

Four 200–250 mg fractions of visually clear garnet and two 250 mg of bulk rock were prepared from sample MW07AL-1 for isotopic analysis. For the whole-rock analyses, one was prepared by partial digestion by hotplate dissolution in a Savillex beaker and one prepared by complete digestion in a sample bomb. All data together yield an isochron age of 132.1 ± 2.4 Ma (2σ), with an MSWD of 5.8 (Fig. 15), which is our preferred age for this sample. Exclusion of either the Savillex or bomb whole rock in the isochron calculation does not change the resulting isochron age within error (132.4 ± 3.5 and 131.9 ± 3.9 Ma, respectively). We determined two-point garnet–whole-rock ages for each garnet fraction using the $^{176}Hf/^{177}Hf$ and $^{176}Lu/^{177}Hf$ ratios for the garnet fraction and for the Savillex whole rock to assess potential intrasample garnet age variability. Garnet–whole-rock isochron ages for the

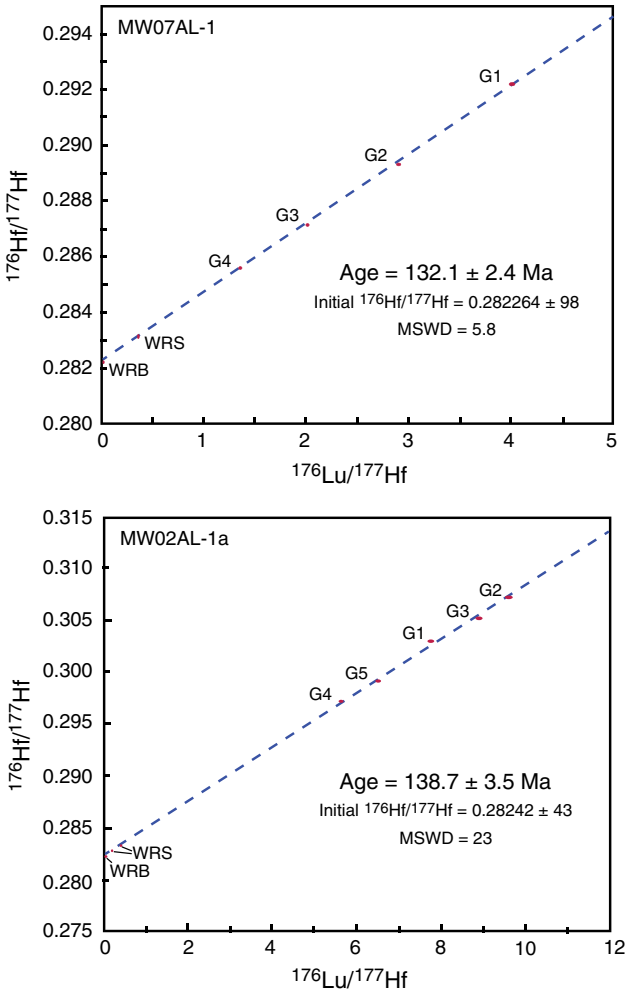

Fig. 15 Lu–Hf isochrons for two samples of the schist of Willow Creek: samples MW07AL-1 and MW02AL-1a. *G* garnet, *WRB* whole-rock bomb, *WRS* whole-rock Savillex. Data in Table 3

garnet fractions are 132.6 ± 1.0 (G1), 130.3 ± 1.6 (G2), 132.7 ± 2.5 (G3), and 130.0 ± 1.2 (G4) (Table 3; Fig. 15), identical within analytical error.

For sample MW02AL-1a, we processed seven garnet fractions and four whole-rock fractions (two bomb, two Savillex). Two of the garnet fractions showed high interferences and are not further considered in our analysis. All data (five garnet fractions and four whole-rock fractions) taken together yield an age of 140.7 ± 2.9 Ma with an initial $^{176}Hf/^{177}Hf$ of 0.28224 ± 4 but with an elevated MSWD (54). The whole-rock bomb analyses plot below the isochron and have elevated Hf contents (5.5–6.2 ppm), consistent with incorporation of unradiogenic Hf from detrital zircons (Scherer et al. 2000), and are excluded from our preferred isochrons. To test for sensitivity of included or excluded garnet aliquots to calculated isochron age, various combinations of isochrons with three or more garnet fractions and one or more whole-rock fractions yield isochron ages varying from 141.4 ± 4.2 to 137.8 ± 0.5 Ma; we use the isochron age from all five garnet fractions and two whole-rock Savillex fractions of 138.7 ± 3.5 (MSWD = 23) as our preferred age (Fig. 15). Garnet–whole-rock ages for each garnet fraction, using the whole-rock Savillex analysis with the lowest $^{176}Lu/^{177}Hf$ ratio, are 141.8 ± 0.8 (G1), 137.9 ± 0.7 (G2), 137.7 ± 0.7 (G3), 140.7 ± 0.8 (G4), and 137.8 ± 0.8 (G5) (Table 3; Fig. 15).

The interpretation of the significance of an age in relation to the *P–T* path depends on where the Lu is hosted in the garnets. Because Lu partitioning in garnet is similar to that of Y (Hickmott et al. 1987), the distribution of Y is a good indication of the Lu distribution. The X-ray maps of Y (Fig. 4) show that the principal Y reservoir (and presumed Lu reservoir) resides in the garnet core for three of the four garnets analyzed. However, considering the small volume of the core relative to the larger volume of the rim (e.g., Kohn 2009), large concentrations of Lu in the core are diluted by rim concentrations. Thus, we interpret the isochron ages of 132.1 ± 2.4 and 138.7 ± 3.5 Ma to date a mixture of Segments *I* and *III* of the composite *P–T* path.

Tectonic significance

The N-shaped *P–T* path described here provides another example of alternations in contraction and extension that serve to modulate crustal thickness within the hinterland of orogenic belts during plate convergence. Kinematic alternations, or tectonic mode switches, have been interpreted in the context of cycles of slab rollback followed by enhanced plate coupling due to slab shallowing or accretion (e.g., Lister et al. 2001; Collins 2002), or delamination cycles (e.g., Wells et al. 2012). In contrast, the relatively small magnitude of exhumation (~3 km) associated with the Early Cretaceous N-shaped *P–T* path documented here (Segment *II*) is more consistent with a response to a perturbation in orogenic wedge mechanics, such as development of supercritical taper by internal wedge thickening or underplating, or rheological weakening (Davis et al. 1983; Platt 1986; Willett 1992). Alternatively, the decompression may record erosional exhumation following shortening-related topographic and relief development superimposed on punctuated shortening. In either case, the N-shaped *P–T* path shows that orogenic processes are not always steady state but rather have more complex, punctuated histories.

Our *P–T* path from the schist of Willow Creek in the hanging wall of the BEF is similar to the path derived by Harris et al. (2007) from the schist of Mahogany Peaks in the footwall (Fig. 16). The footwall path has been recently dated using Lu–Hf garnet geochronology; two samples of the schist of Mahogany Peaks in the Albion Mountains (Fig. 3) yielded ages of 138.7 ± 0.7 and 132 ± 5 Ma

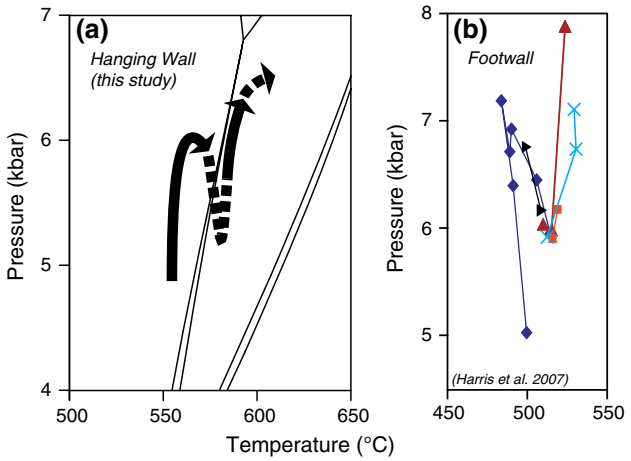

Fig. 16 Comparison of *P–T* paths from the hanging wall and footwall of the Basin-Elba fault. The footwall paths were constructed from garnet chemical zoning by Harris et al. (2007). Differences in absolute *P–T* conditions between hanging wall and footwall rocks can be attributed to differences in rock bulk composition, modeling techniques, thermodynamic data, and activity models. Note different pressure scales

(Cruz-Uribe et al. 2015). The similarities in the *P–T* paths and in the timing of garnet growth between the footwall (Harris et al. 2007; Cruz-Uribe et al. 2015) and hanging wall (this study) of the BEF suggest that they share the same tectonic history during garnet growth. We view three structures as potential causes for tectonic burial that are not mutually exclusive: (1) Burial is due to crustal thickening associated with development of a major fold nappe represented by the >3.4 km of preserved overturned Cambrian to Neoproterozoic rocks of the Mount Harrison sequence. The magnitude of crustal thickening associated with this structure is unknown as the full thickness of the fold nappe is uncertain. (2) The low-angle fault separating the Robinson Creek sequence from the Mount Harrison sequence may represent a thrust responsible for burial (Fig. 2). The Robinson Creek sequence is largely upright, allowing the possibility that it represents the upper limb of the fold nappe that has been displaced along a thrust fault near its axial surface; alternatively, it may represent a thrust of large displacement (Miller 1983). (3) A major structure(s) may lie to the west, presently covered and obscured by Quaternary basin fill, Tertiary volcanic and sedimentary rocks, and upper Paleozoic to Triassic rocks.

Our current understanding of the history of motion along the BEF, together with the newly dated N-shaped *P–T* path in this study, suggests that the Early Cretaceous events occurred prior to thrust juxtaposition along the BEF. Motion along the BEF is thought to have occurred during two stages separated by a period of extensional exhumation: an early stage of Late Cretaceous (~85 Ma) motion and latest Cretaceous to Early Eocene thrust reactivation. The earlier period of BEF motion is recorded in near isothermal, compressional *P–T* paths from the schist of Stevens Spring in Basin Creek dated at ca. 85 Ma by Lu–Hf garnet geochronology (Hoisch et al. 2002; Wells et al. 2012) (Fig. 2). The second period of motion along the BEF is recorded by latest Cretaceous to Early Eocene garnet growth in the schist of Stevens Spring at Basin Creek (Hoisch et al. 2008; Wells et al. 2012) and early Eocene garnet growth in the schist of Upper Narrows at the Upper Narrows (Fig. 2) (Lacy et al. 2014; Lacy 2014). Decompression (~3 kbar) and heating between these burial paths define an N-shaped *P–T* path of latest Cretaceous to Early Eocene age (Hoisch et al. 2002; Wells et al. 2012). The new Early Cretaceous *P–T* path in this study predates these two periods of thrust motion along the BEF, contrary to the previous *P–T* path correlation (Harris et al. 2007) made prior to geochronologic constraints on garnet growth and the recognition that the hanging wall shared the same Early Cretaceous *P–T* path as the footwall.

The Sevier orogeny was the first tectonic event to structurally bury the Cordilleran passive margin strata of the Raft River–Albion–Grouse Creek Mountains—tectonic burial related to earlier Paleozoic and Early Mesozoic orogenesis is restricted to areas to the west in central Nevada. The 7–15 km of structural burial required to bring the schist of Willow Creek from a stratigraphic burial depth of 10–14 to 21–25 km depths recorded in the peak pressure conditions of ~6 kbar must be entirely of Sevier age. Tectonic burial was ongoing in the Early Cretaceous, as indicated by the Valanginian Lu–Hf garnet ages reported here and in Cruz-Uribe et al. (2015). Early Cretaceous crustal shortening supports a protracted Late Jurassic to Early Cenozoic deformation history for the Sevier orogeny in which initial shortening propagated to the east through time as the wedge lengthened (e.g., Davis et al. 1983), rather than a two-stage history (e.g., Smith et al. 1993). This is further supported by a Late Jurassic (158 Ma) Lu–Hf age obtained from garnets that preserve steep *P–T* paths indicative of thrust burial in the Funeral Mountains of southeastern California (Hoisch et al. 2014), representing the earliest evidence of deep thrust burial associated with Sevier orogenesis.

Conclusions

Metamorphic rocks may follow complex *P–T* paths during orogenesis, but some commonly employed methods of *P–T* path construction may not capture sufficient complexity for robust tectonic interpretations. Here we have used garnet chemical zoning in conjunction with evidence for a garnet growth hiatus and changes in phase assemblages and reactions affecting garnet growth to describe Early Cretaceous

metamorphism during early Sevier orogenesis that was accompanied by alternations in pressure. The Lu–Hf garnet ages provide evidence of Early Cretaceous crustal thickening to suggest that shortening during the Sevier Orogeny was continuous rather than two stage, and we interpret the N-shaped *P–T* path as the result of tectonic mode switching, consistent with other evidence in the Sevier hinterland for synorogenic extension. Garnet *P–T* paths from other orogenic belts may also preserve evidence for tectonic mode switching. However, methods that ignore or simplify detailed changes in chemical zoning may overlook important characteristics that reveal fundamental tectonic processes.

Acknowledgments We thank J. Wittke for assistance in collecting EPMA data at NAU, and D. Wilford for assistance with the Lu–Hf garnet dating at WSU. We also thank W. Carlson and his research group for constructive discussions that significantly improved the interpretation of the garnet growth history. Two anonymous reviewers are thanked for providing helpful comments. This work was funded by a Geological Society of America grant to EDK and by National Science Foundation grant EAR-9805076 to TDH, EAR-061009 to MLW, and EAR-0609856 to JDV.

References

Ague JJ, Carlson WD (2013) Metamorphism as garnet sees it: the kinetics of nucleation and growth, equilibration, and diffusional relaxation. Elements 9:439–445

Anczkiewicz R, Szczepanski J, Mazur S, Storey CD, Crowley Q, Villa IM, Thirlwall MF, Jeffries TE (2007) Lu-Hf geochronology and trace element distribution in garnet; implications for uplift and exhumation of ultra-high pressure granulites in the Sudetes, SW Poland. Lithos 95:363–380

Armstrong RL (1968a) Sevier orogenic belt in Nevada and Utah. Geol Soc Am Bull 79:429–458

Armstrong RL (1968b) Mantled gneiss domes in the Albion Range, southern Idaho. Geol Soc Am Bull 79:1295–1314

Armstrong RL (1982) Cordilleran metamorphic core complexes; from Arizona to southern Canada. Annu Rev Earth Planet Sci 10:129–154

Berg CA, Carlson WD, Connelly JN (2013) Strain rates at high temporal resolution from curved inclusion trails in garnet, Passo del Sole, central Swiss Alps. J Metamorph Geol 31:243–262

Bouvier A, Vervoort JD, Patchett PJ (2008) The Lu–Hf and Sm–Nd isotopic composition of CHUR: constraints from unequilibrated chondrites and implications for the bulk composition of terrestrial planets. Earth Planet Sci Lett 273:48–57

Caddick MJ, Konopasek J, Thompson AB (2010) Preservation of garnet growth zoning and the duration of prograde metamorphism. J Petrol 51:2327–2347

Camilleri PA, Chamberlain KR (1997) Mesozoic tectonics and metamorphism in the Pequop Mountains and Wood Hills region, Northeast Nevada; implications for the architecture and evolution of the Sevier Orogen. Geol Soc Am Bull 109:74–94

Carlson WD (2006) Rates of Fe, Mg, Mn, and Ca diffusion in garnet. Am Mineral 91:1–11

Carlson WD (2011) Porphyroblast crystallization: linking mechanisms, kinetics, and microstructures. Int Geol Rev 53:406–445

Carlson WD, Pattison DRM, Caddick MJ (2015) Beyond the equilibrium paradigm: how consideration of kinetics enhances metamorphic interpretation. Am Mineral. doi:10.2138/am-2015-5097

Cheng H, King RL, Nakamura E, Vervoort JD, Zhou Z (2008) Coupled Lu–Hf and Sm–Nd geochronology constrains garnet growth in ultra-high-pressure eclogites from the Dabie orogen. J Metamorph Geol 26:741–758

Cirrincione R, Ortolano G, Pezzino A, Punturo R (2008) Poly-orogenic multi-stage metamorphic evolution inferred via P–T pseudosections; an example from Aspromonte Massif basement rocks (southern Calabria, Italy). Lithos 103:466–502

Collins WJ (2002) Hot orogens, tectonic switching, and creation of continental crust. Geology 30:535–538

Cruz-Uribe AM, Hoisch TD, Wells ML, Vervoort JD, Mazdab FK (2015) Linking thermodynamic modeling, Lu–Hf geochronology, and trace elements in garnet: new *P–T–t* paths from the Sevier hinterland. J Metamorph Geol. doi:10.1111/jmg.12151

Cutts KA, Stevens G, Hoffmann JE, Buick IS, Frei D, Muenker C (2014) Paleo- to Mesoarchean polymetamorphism in the Barberton granite-greenstone belt, South Africa; constraints from U–Pb monazite and Lu–Hf garnet geochronology on the tectonic processes that shaped the belt. Geol Soc Am Bull 126:251–270

Davis D, Suppe J, Dahlen FA (1983) Mechanics of fold-and-thrust belts and accretionary wedges. J Geophys Res 88:1153–1172

de Capitani C, Brown TH (1987) The computation of chemical equilibrium in complex systems containing non-ideal solutions. Geochim Cosmochim Acta 51:2639–2652

de Capitani C, Petrakakis K (2010) The computation of equilibrium assemblage diagrams with Theriak/Domino software. Am Mineral 95:1006–1016

DeCelles PG (2004) Late Jurassic to Eocene evolution of the Cordilleran thrust belt and foreland basin system, western U.S.A. Am J Sci 304:105–168

Dorfler KM, Tracy RJ, Caddick MJ (2014) Late-stage orogenic loading revealed by contact metamorphism in the northern Appalachians, New York. J Metamorph Geol 32:113–132

Dragovic B, Samanta LM, Baxter EF, Selverstone J (2012) Using garnet to constrain the duration and rate of water-releasing metamorphic reactions during subduction: an example from Sifnos, Greece. Chem Geol 314–317:9–22

England PC, Houseman G (1989) Extension during continental convergence, with application to the Tibetan Plateau. J Geophys Res 94:17561–17579

England PC, Thompson AB (1984) Pressure–temperature–time paths of regional metamorphism I. Heat transfer during the evolution of regions of thickened continental crust. J Petrol 25:894–928

Farber K, Caddick M, John T (2014) Controls on solid-phase inclusion during porphyroblast growth: insights from the Barrovian sequence (Scottish Dalradian). Contrib Mineral Petrol 168:1089–1106

Florence FP, Spear FS (1993) Influences of reaction history and chemical diffusion on P–T calculations for staurolite schists from the Littleton Formation, northwestern New Hampshire. Am Mineral 78:345–359

Gaidies F, de Capitani C, Abart R (2008a) THERIA_G: a software program to numerically model prograde garnet growth. Contrib Mineral Petrol 155:657–671

Gaidies F, de Capitani C, Abart R, Schuster R (2008b) Prograde garnet growth along complex P–T–t paths: results from numerical experiments on polyphase garnet from the Wolz Complex (Austroalpine basement). Contrib Mineral Petrol 155:673–688

Harris CR (2003) A pressure–temperature path record of repeated thrusting and exhumation in the Sevier hinterland, Albion Mountains, Idaho. Thesis, Northern Arizona University

Harris CR, Hoisch TD, Wells ML (2007) Construction of a composite pressure–temperature path: revealing the synorogenic burial and exhumation history of the Sevier hinterland, USA. J Metamorph Geol 25:915–934

Hickmott DD, Shimizu N, Spear FS, Selverstone J (1987) Trace-element zoning in a metamorphic garnet. Geology 15:573–576

Hodges KV, Walker JD (1992) Extension in the Cretaceous Sevier orogen, North American. Geol Soc Am Bull 104:560–569

Hoisch TD, Wells ML, Hanson LM (2002) Pressure–temperature paths from garnet-zoning: evidence for multiple episodes of thrust burial in the hinterland of the Sevier orogenic belt. Am Mineral 87:115–131

Hoisch TD, Wells ML, Grove M (2008) Age trends in garnet-hosted monazite inclusions from upper amphibolite facies schist in the northern Grouse Creek Mountains, Utah. Geochim Cosmochim Acta 72:5505–5520

Hoisch TD, Wells ML, Beyene MA, Styger S, Vervoort JD (2014) Jurassic Barrovian metamorphism in a Western U.S. cordilleran metamorphic core complex, Funeral Mountains California. Geology 42:399–402

Holland TJB, Powell R (1998) An internally consistent thermodynamic data set for phases of petrological interest. J Metamorph Geol 16:309–343

Jamieson RA, Beaumont C (2011) Coeval thrusting and extension during lower crustal ductile flow—implications for exhumation of high-grade metamorphic rocks. J Metamorph Geol 29:33–51

Kelly ED, Carlson WD, Ketcham RA (2013) Magnitudes of departures from equilibrium during regional metamorphism of porphyroblastic rocks. J Metamorph Geol 31:981–1002

Kohn MJ (1993) Uncertainties in differential thermodynamic (Gibbs' method) P–T paths. Contrib Mineral Petrol 113:24–39

Kohn MJ (2009) Models of garnet differential geochronology. Geochim Cosmochim Acta 73:170–182

Kohn MJ, Spear FS (1991) Error propagation for barometers: 2. Application to rocks. Am Mineral 76:138–147

Lacy AC (2014) Garnet dating, pressure-temperature-time paths and kinematic analysis of the schist of Upper Narrows, Raft River Mountains, Northwestern Utah: tectonic implications of pressure-temperature-time-deformation paths. Thesis, University of Nevada, Las Vegas

Lacy AC, Wells ML, Hoisch TD, Vervoort JD (2014) Early Eocene tectonic mode switching in the hinterland of the Sevier orogenic belt evidenced by thermodynamic modeling and kinematic analysis of garnets in the schist of Upper Narrows, Raft River Mountains, northwestern Utah. Geol Soc Am Abstr Programs 46:6

Lang HM (1996) Pressure–temperature–reaction history of metapelitic rocks from the Maryland Piedmont on the basis of correlated garnet zoning and plagioclase-inclusion composition. Am Mineral 81:1460–1475

Lister GS, Forster MA, Rawling TJ (2001) Episodicity during orogenesis. Geol Soc Lond Spec Publ 184:89–113

Miller DM (1978) Deformation associated with Big Bertha Dome, Albion Mountains, Idaho. Dissertation, University of California, Los Angeles

Miller DM (1980) Structural geology of the northern Albion Mountains. Geol Soc Am Mem 153:399–423

Miller DM (1983) Allochthonous quartzite sequence in the Albion Mountains, Idaho, and proposed Proterozoic Z and Cambrian correlatives in the Pilot Range, Utah and Nevada. Geol Soc Am Mem 157:191–213

Moore SJ, Carlson WD, Hesse MA (2013) Origins of yttrium and rare earth element distributions in metamorphic garnet. J Metamorph Geol 31:663–689

Moynihan DP, Pattison DRM (2013a) An automated method for the calculation of P–T paths from garnet zoning, with application to metapelitic schist from the Kootenay Arc, British Columbia, Canada. J Metamorph Geol 31:525–548

Moynihan DP, Pattison DRM (2013b) Barrovian metamorphism in the central Kootenay Arc, British Columbia; petrology and isograd geometry. Can J Earth Sci 50:769–794

Nabelek PI, Chen Y (2014) The initial garnet-in reaction involving siderite-rhodochrosite, garnet re-equilibration and P–T–t paths of graphitic schists in the Black Hills Orogen, South Dakota, USA. J Metamorph Geol 32:133–150

Pattison DRM, Tinkham DK (2009) Interplay between equilibrium and kinetics in prograde metamorphism of pelites: an example from the Nelson aureole, British Columbia. J Metamorph Geol 27:249–279

Pattison DRM, De Capitani C, Gaidies F (2011) Petrological consequences of variations in metamorphic reaction affinity. J Metamorph Geol 29:953–977

Platt JP (1986) Dynamics of orogenic wedges and the uplift of high-pressure metamorphic rocks. Geol Soc Am Bull 97:1037–1053

Powell R, Holland TJB (2008) On thermobarometry. J Metamorph Geol 26:155–179

Pyle JM, Spear FS (1999) Yttrium zoning in garnet; coupling of major and accessory phases during metamorphic reactions. Geol Mater Res 1:1–49

Rey P, Vanderhaeghe O, Teyssier C (2001) Gravitational collapse of the continental crust: definition, regimes and modes. Tectonophysics 342:435–449

Rubie DC (1998) Disequilibrium during metamorphism: the role of nucleation kinetics. Geol Soc Lond Spec Publ 138:199–214

Saltzer SD, Hodges KV (1988) The Middle Mountain shear zone, southern Idaho: kinematic analysis of an early Tertiary high-temperature detachment. Geol Soc Am Bull 100:96–103

Scherer EE, Cameron KL, Blichert-Toft J (2000) Lu–Hf geochronology: closure temperature relative to the Sm–Nd System and the effects of trace mineral inclusions. Geochim Cosmochim Acta 64:3413–3432

Scherer E, Münker C, Mezger K (2001) Calibration of the lutetium–hafnium clock. Science 293:683–687

Selverstone J, Spear FS (1985) Metamorphic P–T paths from pelitic schists and greenstones from the south-west Tauern Window, Eastern Alps. J Metamorph Geol 3:439–465

Skora S, Baumgartner LP, Mahlen NJ, Johnson CM, Pilet S, Hellebrand E (2006) Diffusion-limited REE uptake by eclogite garnets and its consequences for Lu/Hf and Sm/Nd geochronology. Contrib Mineral Petrol 152:703–720

Smith DL, Miller EL, Wyld SJ, Wright JE (1993) Progression and timing of Mesozoic crustal shortening in the northern Great Basin, western U.S.A. In: Dunn G, McDougall K (eds) Mesozoic paleogeography of the Western United States–II, vol 71. Pacific Section Society of Economic Paleontologist and Mineralogists Book, pp 389–406

Söderlund W, Patchett PJ, Vervoort JD, Isachsen CE (2004) The ^{176}Lu decay constant determined by Lu–Hf and U–Pb isotope systematics of Precambrian mafic intrusions. Earth Planet Sci Lett 219:311–324

Spear FS (1995) Metamorphic phase equilibria and pressure–temperature–time paths. Min Soc Am Monograph, Washington

Spear FS, Pyle JM (2010) Theoretical modeling of monazite growth in a low Ca metapelite. Chem Geol 273:111–119

Spear FS, Selverstone J, Hickmott D, Crowley P, Hodges KV (1984) P–T paths from garnet zoning: a new technique for deciphering tectonic processes in crystalline terranes. Geology 12:87–90

Spear FS, Kohn MJ, Florence FP, Menard T (1990) A model for garnet and plagioclase growth in pelitic schists; implications for thermobarometry and P–T path determinations. J Metamorph Geol 8:683–696

Spear F, Thomas J, Hallett B (2014) Overstepping the garnet isograd: a comparison of QuiG barometry and thermodynamic modeling. Contrib Mineral Petrol 168:1–15

Stowell HH, Tinkham DK (2003) Integration of phase equilibria modelling and garnet Sm–Nd chronology for construction of P–T–t paths: examples from the Cordilleran Coast Plutonic Complex, USA. Geol Soc Lond Spec Publ 220:119–145

Stowell H, Bulman G, Tinkham D, Zuluaga C (2011) Garnet growth during crustal thickening in the Cascades Crystalline Core, Washington, USA. J Metamorph Geol 29:627–647

Tinkham DK, Ghent ED (2005) Estimating P–T conditions of garnet growth with isochemical phase diagram sections and the problem of effective bulk composition. Can Mineral 43:35–50

Todd CS (1998) Limits on the precision of geobarometry at low grossular and anorthite content. Am Mineral 83:1161–1167

Vervoort JD, Blichert-Toft J (1999) Evolution of the depleted mantle: Hf isotope evidence from juvenile rocks through time. Geochim Cosmochim Acta 63:533–556

Vervoort JD, Patchett PJ, Söderlund U, Baker M (2004) Isotopic composition of Yb and the determination of Lu concentrations and Lu/Hf ratios by isotope dilution using MC-ICPMS. Geochem Geophys Geosyst 5:1–15

Vorhies SH, Ague JJ (2011) Pressure–temperature evolution and thermal regimes in the Barrovian zones, Scotland. J Geol Soc 168:1147–1166

Vrijmoed JC, Hacker BR (2014) Determining P–T paths from garnet zoning using a brute-force computational method. Contrib Mineral Petrol 167:1–13

Waters DJ, Lovegrove DP (2002) Assessing the extent of disequilibrium and overstepping of prograde metamorphic reactions in metapelites from the Bushveld Complex aureole, South Africa. J Metamorph Geol 20:135–149

Wells ML, Sheeley JC, Spell TL, Kelly ED, Hoisch TD (2004) Eocene extension in northwestern Utah-southern Idaho: early motion on the polyphase Middle Mountain shear zone. Geol Soc Am Abstr Programs 36:73

Wells ML, Hoisch TD, Cruz Uribe AM, Vervoort JD (2012) Geodynamics of synconvergent extension and tectonic mode switching; constraints from the Sevier-Laramide Orogen. Tectonics 31:TC1002

Whitney DL, Evans BW (2010) Abbreviations for names of rock-forming minerals. Am Mineral 95:185–187

Wilbur DE, Ague JJ (2006) Chemical disequilibrium during garnet growth: Monte Carlo simulations of natural crystal morphologies. Geology 34:689

Willett SD (1992) Dynamic and kinematic growth and change of a Coulomb wedge. In: McClay KR (ed) Thrust Tectonics. Chapman and Hall, London, pp 19–31

Zeh A, Holness MB (2003) The effect of reaction overstep on garnet microtextures in metapelitic rocks of the Ilesha Schist Belt, SW Nigeria. J Petrol 44:967–994

Zeh A, Millar IL (2001) Metamorphic evolution of garnet–epidote–biotite gneiss from the Moine Supergroup, Scotland, and geotectonic implications. J Petrol 42:529–554

Zeh A, Klemd R, Barton JM (2005) Petrological evolution in the roof of the high-grade metamorphic Central Zone of the Limpopo Belt, South Africa. Geol Mag 142:229–240

Zuluaga CA, Stowell HH, Tinkham DK (2005) The effect of zoned garnet on metapelite pseudosection topology and calculated metamorphic P–T paths. Am Mineral 90:1619–1628